Spectral Modulation Interferometry: A high-sensitivity, high-speed approach to quantitative phase imaging

Ruibo Shang

Thesis submitted to the faculty of the Virginia Polytechnic Institute and State University in partial fulfillment of the requirements for the degree of

Master of Science
In
Electrical and Computer Engineering

Yizheng Zhu, Chair
Yong Xu
Masoud Agah

May 4, 2015
Blacksburg, VA

Keywords: Interference microscopy, Interferometric imaging, Coherence imaging, Phase measurement

Spectral Modulation Interferometry: A high-sensitivity, high-speed approach to quantitative phase imaging

Ruibo Shang

ABSTRACT

Many biological specimens are transparent and in weak intensity contrast, making it invisible using conventional bright field microscopes. Therefore, the phase-based optical microscopy techniques play important roles in the development of the modern biomedical science. Furthermore, the ability to achieve quantitative phase measurement of the tiny structures of biomedical specimens is of great importance for many biomedical applications. Thus, quantitative phase imaging becomes an important technique to measure the phase variations due to the difference of refractive index and geometric thickness of various structures and materials within the biomedical specimens.

In this thesis, a spectral modulation interferometry (SMI) is developed to achieve quantitative phase imaging. In SMI, the phase and amplitude information will simultaneously be modulated onto the interference spectrum of the broadband light. Full-field phase images can be obtained by scanning along the orthogonal direction only. SMI incorporates the advantages of low coherence from broadband light source, high sensitivity from spectral domain interferometry and the high speed from the spectral modulation technique to achieve quantitative phase measurement with free of speckle, high temporal sensitivity (~0.1nm) and fast imaging rate. The principles of SMI system and programming as well as some important image processing methods will be discussed in detail. Besides, the quantitative phase measurement of the reflective object (USAF resolution target) and the transmitted biological objects (Peranema, human cheek cells) will be shown.

Acknowledgement

This research work will not be accomplished without the encouragement and support from Dr. Yizheng Zhu, who offers me an opportunity to pursue my Master at Center for Photonic Technology. In the past two years, he helped me improve my research skills. With his constant support, two papers based on this research work were published with high quality. I would like to express my sincere appreciation for his advising. I would also like to say thanks to all the committee members of the thesis defense, Dr. Yong Xu and Dr. Masoud Agah, for their unreserved advices and help in this research work.

In the past two years, I spent my research time in Center for Photonic Technology. To all the students in CPT, I would like to thank them for their help and advices in my research. Especially, I would like to express my appreciation to Shichao Chen and Chengshuai Li in our lab for their sincere technical help and friendship in life. I am happy that I can spend two years here to improve my technical and communication skills. This will be the memory that I will remember forever.

This work was supported in part by a Junior Faculty Collaborative grant from the Institute for Critical Technology and Applied Science (ICTAS) at Virginia Tech.

Table of Contents

List of Figures

Chapter 1

Introduction

Ever since it was invented, quantitative phase imaging (QPI) has played more and more important roles in modern biomedical research. By quantifying the phase distribution of the measured specimens, the application of QPI covers the fields of cellular morphology, surface metrology and bio-dynamic detection [1-4]. In this chapter, the basic concepts in phase imaging especially QPI and the judgment of the performance of QPI have been demonstrated. Besides, several types of QPI techniques have been introduced.

1.1 Phase imaging

Firstly, the definition of phase in optical imaging and the importance of phase measurement are demonstrated here.

1.1.1 Definition of phase term in optical imaging

In electromagnetic theorem, the phase is an important term to reflect the properties of the waves. The phase term comes from solving the Maxwell's equation [5] as shown in Eq. (1-1)

$$\begin{aligned} \nabla \bullet \vec{D} &= \rho_v \\ \nabla \bullet \vec{B} &= 0 \\ \nabla \times \vec{E} &= -\frac{\partial \vec{B}}{\partial t} \\ \nabla \times \vec{H} &= \vec{J}_c + \frac{\partial \vec{D}}{\partial t} \end{aligned} \tag{1-1}$$

By taking the curl on both sides of the third and fourth equation in Eq. (1-1) respectively, we can get the vector wave equations with source as shown in Eq. (1-2),

$$\nabla^2 \vec{E} - \mu_0 \varepsilon_0 \frac{\partial^2 \vec{E}}{\partial t^2} = \mu_0 \frac{\partial \vec{J}_c}{\partial t} + \nabla(\frac{\rho_v}{\varepsilon_0})$$
$$\nabla^2 \vec{H} - \mu_0 \varepsilon_0 \frac{\partial^2 \vec{H}}{\partial t^2} = -\nabla \times \vec{J}_c \quad (1\text{-}2)$$

Especially for free space, Eq. (1-2) becomes,

$$\nabla^2 \vec{E} - \mu_0 \varepsilon_0 \frac{\partial^2 \vec{E}}{\partial t^2} = 0$$
$$\nabla^2 \vec{H} - \mu_0 \varepsilon_0 \frac{\partial^2 \vec{H}}{\partial t^2} = 0 \quad (1\text{-}3)$$

For solving the vector wave equation for the electric field, the Cartesian coordinate is used to present the electric field in x, y and z direction as E_x, E_y and E_z. Then, apply it to the first equation in Eq. (1-3), we can get the 3D scalar wave equation,

$$\nabla^2 \varphi = \mu_0 \varepsilon_0 \frac{\partial^2 \varphi}{\partial t^2} = \frac{1}{v^2} \frac{\partial^2 \varphi}{\partial t^2} \quad (1\text{-}4)$$

Thus, the solutions to Eq. (1-4) tell us about the distribution of electric field. A general solution to the 3D scalar wave equation is,

$$\varphi(x, y, z, t) = c_1 f(\omega_0 t - (k_{ox} x + k_{oy} y + k_{oz} z)) + c_2 g(\omega_0 t + (k_{ox} x + k_{oy} y + k_{oz} z)) \quad (1\text{-}5)$$

Therefore, the phase of the wave is defined as,

$$Phase = k_{ox} x + k_{oy} y + k_{oz} z = \vec{k}_0 \bullet \vec{R}$$
$$\vec{k}_0 = k_{ox} \hat{x} + k_{oy} \hat{y} + k_{oz} \hat{z}$$
$$\vec{R} = x \hat{x} + y \hat{y} + z \hat{z} \quad (1\text{-}6)$$

where the resonant time term is neglected.

Since the light is also a form of electromagnetic waves. The whole equations to solve the light propagation issues are the same as those in the electromagnetic theorem. The corresponding solution describes the wave optics.

In optical imaging, phase is also an important term to reflect the properties of the samples such as the surface profile, the thickness of the samples or the distribution of the reflective index. However, since the phase of the field varies at the optical period, the absolute phase cannot be

directly measured due to the limit of the response time of the measurement tools. Therefore, the phase difference between the two fields is usually measured to represent the relative phase with one field as the reference. The main method to generate phase difference between the fields is by introducing interference in the experiment. Therefore, most of the optical phase imaging methods are based on the interferometric configuration.

1.1.2 The importance of phase measurement in biomedical research

In terms of imaging, one of the most important factor is the image contrast. Only by contrast can we actually see the obtained image. Usually, the intensity contrast is a good way to make the image to be seen. The differences from spatial reflection or transmission form the intensity contrast, which represents the spatial properties of the measured object. The conventional microscopes are using the intensity contrast to form the image.

However, for biological specimens, the intensity contrast might not be a good tool for imaging since most of them are transparent and in weak intensity contrast. From the intensity image, we actually cannot see its structure. Therefore, in order to get the image of biological specimens which cannot be measured using the conventional bright field microscope, a number of phase-based optical imaging techniques have been developed to render the biological specimen visible, playing an important role in the developing of the biomedical sciences.

One of the most popular phase-based optical imaging techniques is the Zernike phase contrast microscopy [6]. After passing through the condenser annulus and the condenser, the illuminating light will be focused on the specimen. After passing through the specimen, there will be two types of light. One is the scattered light aftering interacting with the specimen. Another one is the unaffected bacground light. Usually, the scattered light will have -90° phase shift. In this case, vector sum of the background and the scattered light (foreground light) will approximately have the same intensity with the background light. Therefore, the contrast will be quite low. In phase contrast microscopy, a -90° phase shift ring is put after the objective to shift the phase of the background light by-90°. Now, the scattered and the background light will have the same phase. The foreground light will be larger than the background light.. Then, a gray filter ring is added after the phase shift ring to dim the intensity of the background light. In this case, the foreground light will be much larger than the background light for better image contrast.

Another popular phase-contrast imaging technique is Differential interference contrast (DIC) microscopy [7] also known as Nomarski interference contrast. DIC systems separate a polarized light source into two orthogonal-polarized, equally-phased, coherent light. These two polarized light are usually spatially separated by Wollaston prism. Then these two tiny separated light beams pass through the sample. Finally, this pair of light beam pass through a polarized filter where they are recombined and generate interference at the image plane. This interference of the two separated polarized light generates the image contrast. Obviously, this contrast is proportional to the path length gradient along the shearing direction, emphasizing the edges of the image, similar to the function of a Laplacian filter to an image.

1.2 Quantitative phase imaging

Although the classic phase contrast microscopy can provide image contrast when dealing with transparent biological specimens, it actually does not measure the phase but only directly convert it to the intensity to be visible under the microscope. The conversion between the intensity and the phase is nonlinear, which cannot provide quantitative phase measurement, resulting in artifacts in the imaging results. For example, for classic phase contrast microscope, there will be halos on the acquired image [8]. Therefore, how to develop QPI techniques is a challenge for the biomedical research.

QPI techniques also rely on the intrinsic phase information of the sample as the contrast mechanism, similar to that of Zernike phase contrast microscopy [6] and Nomarski differential interference contrast microscopy [7,9]. However, different from conventional qualitative phase imaging, in QPI, the small variations in refractive index and geometric thickness of various structures and materials within cells and tissues contribute to the total phase distribution. Therefore, QPI is able to provide both the quantitative phase and amplitude information of the tested biological specimens. The measured phase term will then be converted to the optical pathlength (OPL) to reflect the properties of the measured samples.

In order to quantitatively describe the performance of a certain QPI technique, some parameters are used. The three main parameters are: image acquisition rate, resolution (usually transverse direction) and the sensitivity (both temporal and spatial) [10].

(1) Image acquisition rate

According to the Nyquist-Shannon theorem [11], the sampling frequency should be at least twice the frequency of acquired signal. For some biological specimens, especially the dynamic samples moving at a fast speed, it requires the corresponding QPI technique to have an even faster image acquisition rate. Therefore, the image acquisition rate is an important factor for a QPI technique.

(2) Resolution (transverse direction)

Resolution is another factor to describe the performance of a QPI technique. Actually, it is one factor to describe the performance of all the optical imaging techniques. For phase imaging, we usually do not measure the 3D structure. Therefore, only the transverse resolution is of importance. According to the diffraction theory, all the optical imaging system has a diffraction-limited resolution due to the limited size of the optical components. For most of the QPI system, the maximum achievable frequency of the sample is determined by the numerical aperture of the objective. According to the Nyquist-Shannon theorem, the spatial sampling frequency of the QPI system should be twice of the value. Therefore, how to maintain a high enough spatial sampling frequency is the key to a high resolution.

(3) Sensitivity (temporal and spatial)

The sensitivity of the QPI system describes the smallest detectable phase change. It determines the stability of a given QPI system. Factors such as extrinsic and intrinsic noise, system mechanical fluctuation and environmental disturbance [10] all contribute to the system sensitivity. In order to increase the sensitivity of the system as much as possible, some operations can be done. The first is to stabilize the system mechanically so that the system fluctuation could be reduced. The second is to enhance the signal-to-noise ratio (SNR) to reduce the negative influence of the noise. Besides, the configuration of common path interferometry can be used so that the two fields experience almost the same path to reduce the spatial disturbance. For our SMI system, all these three operations have been considered to increase the system sensitivity.

1.3 Specific types of quantitative phase imaging techniques

Since QPI plays an important role in modern biomedical studies, many types of QPI techniques have been invented by the researchers. Most of the QPI techniques involve the combination of holography, diffraction, phase-shift, etc. with interference configurations, etc [12-16]. The whole

optical systems involve coherent optical system (usually coherent light such as laser as the light source) and the incoherent optical system (usually white-light source). Here, several popular QPI techniques are introduced and described.

1.3.1 Digital Holography

Since the data processing procedures of SMI is similar to that of digital holographic microscopy [17-19], the principles and applications of digital holography are described in detail.

We usually use the photograph to record a 3D image. The photograph only record the intensity information at the recording film so that the phase information of the light is lost. Therefore, the holography was invented, not only to record the intensity information but also the phase information [20]. Actually, the word 'holography' comes from two Greek words where 'holo' means 'complete' and 'graphein' means 'to record'[21]. The corresponding recording film is called' hologram'. By illuminating the hologram, the original 3D image will be reconstructed.

Since optical wave propagation is totally described by diffraction theory, the hologram reconstruction can be done using numerical computation. It was firstly demonstrated by J. W. Goodman, et al that it is possible to numerically reconstruct the hologram [22]. A vidicon detector was used to record the hologram and a PDP-6 computer was used to numerically compute the original 3D image. For conventional on-axis holography, when we view the reconstructed virtual image, we can also see the reconstructed real image, known as the 'twin image' problem [21]. This real image actually has a negative influence to the virtual image as noise. In order to solve this problem, the off-axis holography was demonstrated by Leith and Upatnieks [23] to separate the reconstructed real image and the zero-order beam from the desired image. To achieve the off-axis recording, we can simply rotate the reference mirror so that the reference light will be incident on the film at an angle. When reconstructing the image, we also use the light beam with the same incident angle to illuminate the hologram.

With the development of charge-coupled devices (CCD), most researchers began to use CCD to record the hologram because of its fast speed and accuracy recording. Schnars, et al [24] demonstrated the off-axis digital holography with a CCD as the hologram detector.

It was the first demonstration of combining the off-axis digital holography with CCD detector, similar to the modern digital holography techniques. Later, digital holography was also used to

image the tiny objects with objectives in it. Therefore, digital holography microscopy was demonstrated for nanometer-level accuracy optical thickness measurement.

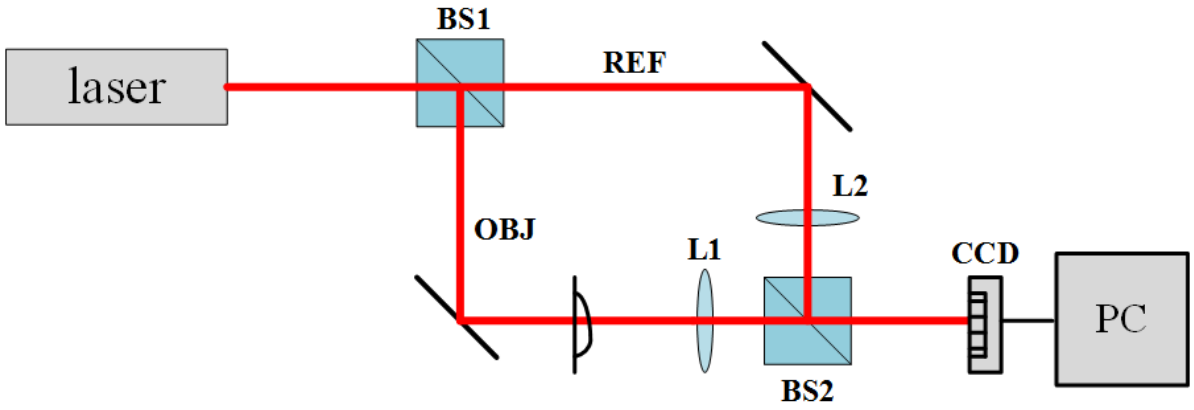

Fig.1-1 Standard configuration of digital holography microscopy

A standard digital homography microscopy will be based on Mach-Zehnder interferometry and will be available both in reflection and transmission types. Fig.1-1 shows a typical digital holography with the reflection type [17,18]. The He-Ne laser is collimated and divided by the beamsplitter into sample beam and reference beam. The sample beam illuminates the object. A pari of similar microscopy objectives are used in two branches for wavefront match and magnification. A CCD camera is put perpendicular to the object at a distance. A slight angle is introduced between the sample and reference arms by means of tilting the beamsplitter (BS2) to achieve off-axis digital holographic configuration. A digital delay generator is used to trigger the laser and the CCD camera simutaneously and a computer is used for processing the acquired image and hologram calculation.

We can see how the digital holography can record the complete information of the sample from its theorem. Suppose the CCD camera is put before the image plane by a distance of d. The sample field is $E_s(x,y)$ and the reference field is $E_r(x,y)$. On the image plane, the field is just an amplified version of the sample field. Therefore, the image field is,

$$E_i(x,y) = \frac{1}{A^2} E_s(\frac{x}{A}, \frac{y}{A}) \tag{1-7}$$

where A is the amplified ratio.

According to the Fresnel diffraction, the sample field on the CCD camera is,

$$E_c(x,y) = E_i(x,y) * e^{-\frac{jk_0}{2d}(x^2+y^2)} \tag{1-8}$$

After interference with the reference field on the CCD camera, the total field and intensity distribution on the CCD camera is,

$$\begin{aligned} E_{total}(x,y) &= E_c(x,y) + |E_r(x,y)| e^{j(k_0 x \sin\theta + k_0 z \cos\theta)} \\ I_{total}(x,y) &= |E_{total}(x,y)|^2 = |E_c(x,y)|^2 + |E_r(x,y)|^2 \\ &\quad + E_c(x,y)|E_r(x,y)|e^{-jk_0 x \sin\theta} + E_c^*(x,y)|E_r(x,y)|e^{jk_0 x \sin\theta} \end{aligned} \tag{1-9}$$

where θ is the off-axis angle.

Then, do Fourier transform of the acquired intensity,

$$I_{total}(k_x,k_y) = I_0(k_x,k_y) + |E_r| E_c(k_x - k_0 \sin\theta, k_y) + |E_r| E_c(k_x + k_0 \sin\theta, k_y) \tag{1-10}$$

After filtering the second term and applying the properties of Gaussian function in Fourier transform, we have,

$$I_1(k_x,k_y) = |E_r| E_s(k_x,k_y) e^{j\frac{d}{2k_0}(k_x^2+k_y^2)} \tag{1-11}$$

Using inverse Fourier transform, we can therefore get the original sample field with both amplitude and phase information.

Besides the conventional digital holography, there are also phase-shift digital holography [25], frequency-shift digital holography [26], etc. The study of digital holography also includes super resolution, optical sectioning, etc.

Some experimental results with digital holographic microscopy for QPI are shown in Fig. 1-2 [18]. From the figure, we can see that the surface profile of a resolution target has been demodulated from digital holographic microscopy. However, since digital holography usually uses laser as the light source, any dust near the object will show in the final demodulated image as the speckle. This is why we see some small bumps on the surface. The speckle problem in digital holography really has a negative influence to the sensitivity of the final phase image. One of the solution is to use low-coherence light as the light source for QPI, which is what we do in SMI. It will be described in detail later.

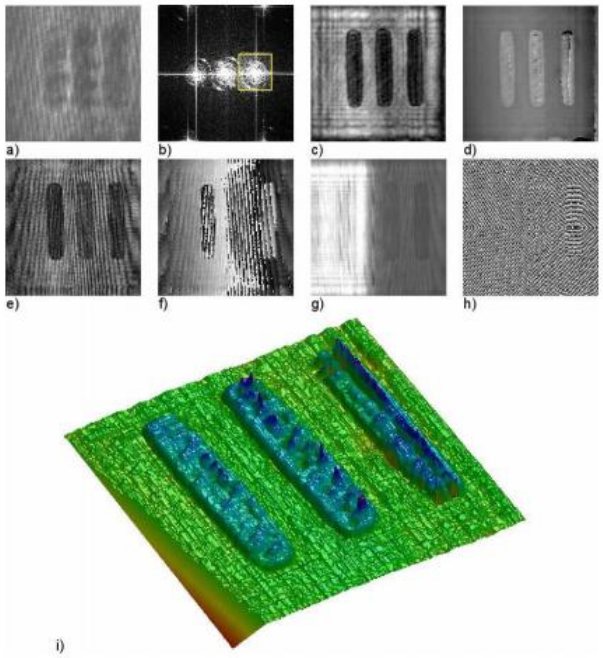

Fig. 1-2 Phase image of the resolution target from digital holographic microscopy [18] C. J. Mann, L. F. Yu, C. M. Lo, and M. K. Kim. "High-resolution quantitative phase-contrast microscopy by digital holography," Optics Express **13**(22), 8693-8698 (2005). Used under fair use, 2015.

1.3.2 Phase-shifting quantitative phase imaging

Some phase-shifting components such as the wave plate and rotated polarizer can also be applied to the optical system for quantitative phase imaging. Fig. 1-3 shows s typical phase-shifting QPI device [27].

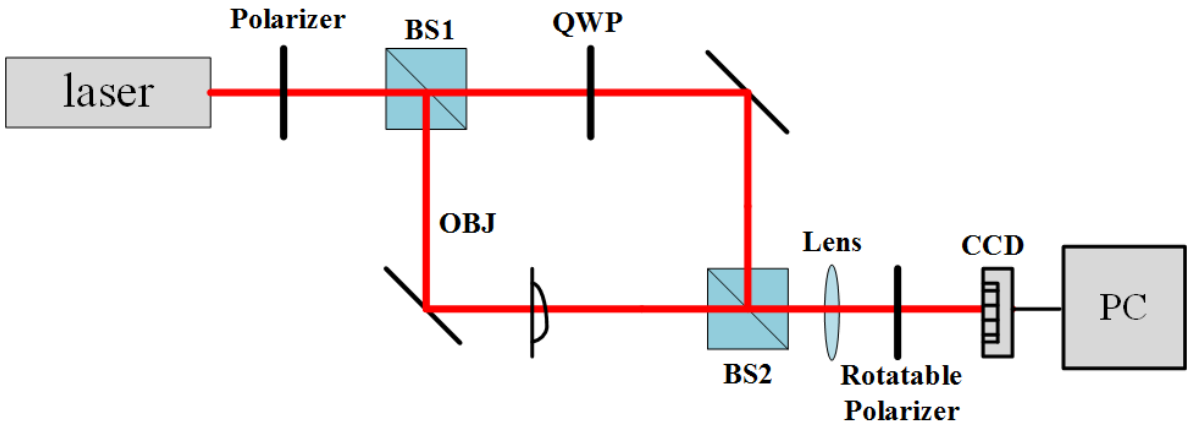

Fig.1-3 Configuration of phase-shifting QPI system

After passing the first polarizer, the He-Ne laser beam will become linear polarized and illuminates the object in the sample arm. For the reference arm, after passing a quarter wave plate, the beam will be circularly polarized. Then, a beam splitter is used to combine the two beams together to form interference. Another polarizer which can be rotated from vertical direction to horizontal direction is put in front of the CCD camera. Thus, the vertical components of the interference pattern will be $\pi/2$ out of phase compared with the horizontal components. With these two measurements in quadrature, the real part (cosine part) and the imaginary part (sine part) of the interference pattern can be obtained. Then, the signal beam amplitude can be obtained by subtracting the reference beam and sample beam intensity from the image and divided by the square root of the reference beam intensity. If this is done with each polarization condition, the total complex field can be obtained.

1.3.3 White-light diffraction quantitative phase microscopy

The diffraction phase microscopy [28] combines the off-axis configuration and the common-path properties. Therefore, it shows the advantages of fast acquisition rate and high sensitivity. The spatial light interference microscopy can almost get rid of the speckle noise using the white light illumination. When combining these two techniques, the white light diffraction quantitative phase microscopy (wDPM) was demonstrated by Popescu, et al[29]. Fig.1-4 shows the configuration of wDPM.

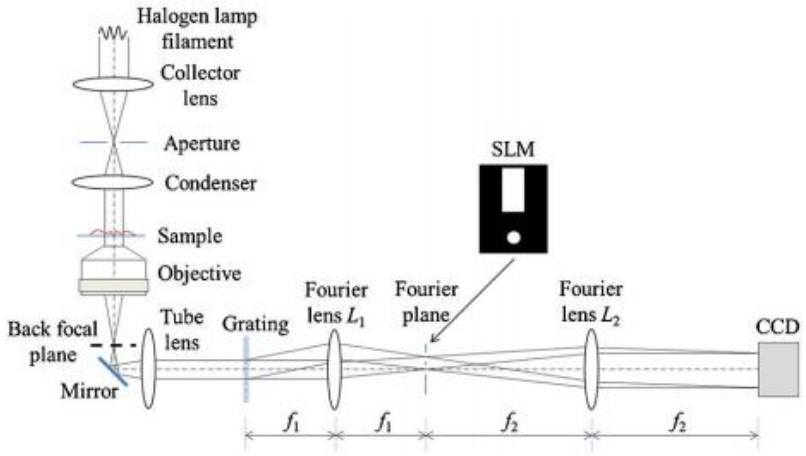

Fig.1-4 Configuration of wDPM [29] B. Bhaduri, H. Pham, M. Mir, and G. Popescu, "Diffraction phase microscopy with white light," Opt. Lett., **37**(6), 1094-1096 (2012). Used under fair use, 2015.

The spatially coherent white light is generated by a commercial Halogen lamp. Then, an aperture is closed to its minimum size so that the field is spatially coherent in the field of view. Then, an amplitude diffraction grating is put in the system so that different diffraction orders containing the spatial information of the sample will be diffracted. With Fourier lens L_1, the zeroth-order and the first-order beam will be separated. With a special shape spatial light modulator, a low-pass filter is applied to the zeroth-order beam so that only the DC term can be acquired while the first-order beam does not have the filter so that it is totally passed. The lens system of L_1 and L_2 works as a Mach-Zehnder interferometer with the first-order beam as the sample field and the zeroth-order beam as the reference field. Finally, a CCD camera is put at the end to receive the interference signal.

1.4 Spectral imaging techniques for biomedical research

In biomedical research, spectral imaging techniques are demonstrated useful for a variety of applications [30, 31]. The optical spectrum after the specimen carries information of its structure, physical parameters, etc. The spectral imaging is usually achieved by the used of gratings and prisms as wavelength dispersion elements [32, 33]. When combining the spectral imaging techniques with low-coherence interferometry, it can provide a creative way to enhance the image acquisition rate while maintaining high temporal and spatial sensitivity, which can be an effective way to detect the dynamic process of the biological specimens. Thus, a spectral-domain interferometric technique, termed spectral modulation interferometry (SMI), is proposed and its application in quantitative phase imaging is demonstrated in this thesis. SMI integrates the high-sensitivity of spectral-domain interferometry with the high-speed of spectral modulation [32-35] to quantify fast phase dynamics of the specimen.

1.5 Reference

1. Y. Park, C. A. Best, T. Auth, N. S. Gov, S. A. Safran, G. Popescu, S. Suresh, and F. S. Feld, "Metabolic remodeling of the human red blood cell membrane," Proc. Natl. Acad. Sci. U. S. A., **107**(4), 1289-1294 (2010).

2. P. Jourdain, N. Pavillon, C. Moratal, D. Boss, B. Rappaz, C. Depeursinge, P. Marquet, and P. J. Magistretti, "Determination of Transmembrane Water Fluxes in Neurons Elicited by Glutamate Ionotropic Receptors and by the Cotransporters KCC2 and NKCC1: A Digital Holographic Microscopy Study," J. Neuroscience **31**(33), 11846-11854 (2011).
3. N. T. Shaked, L. L. Shatterwhite, N. Bursac, and A. Wax, "Whole-cell-analysis of live cardiomyocytes using wide-field interferometric phase microscopy," Biomed. Opt. Express **1**(2), 706-719 (2010).
4. M. Mir, Z. Wang, Z. Shen, M. Bednarz, R. Bashir, I. Golding, S. G. Prasanth, and G. Popescu, "Optical measurement of cycle-dependent cell growth," Proc. Natl. Acad. Sci. U. S. A. **108**(32), 13124-13129 (2011).
5. J. M. Jin, Theory and computation of electromagnetic fields (John Wiley& Sons, 2011).
6. F. Zernike, "Phase contrast, a new method for the microscopic observation of transparent objects," Physica **9**(10), 974-986 (1942).
7. G. Nomarski, "Differential microinterferometer with polarized waves," J. Phys. Radium **16**(9), 9S-11S (1955).
8. T. Otaki, "Artifact halo reduction in phase contrast microscopy using apodization,' Optical Review **7**(2), 119-122 (2000).
9. Y. Z. Zhu, N. T. Shaked, L. L. Satterwhite, and A. Wax, "Spectral-domain differential interference contrast microscopy," Opt. Lett. **36**(4), 430-432 (2011).
10. G. Popescu, *Quantitative phase imaging of cells and tissues* (McGraw-Hill, 2011).
11. C. E. Shannon, "A mathematical theory of communication," Bell System Technical Journal **27**, 379-423, 623-656 (1948).
12. N. T. Shaked, M. T. Rinehart, and A. Wax, "Dual-interference-channel quantitative-phase microscopy of live cell dynamics," Opt. Lett. **34**(6), 767-769 (2009).
13. M. T. Rinehart, J. Volker, and A. Wax, "Quantitative phase microscopy with off-axis optical coherence tomography," Opt. Lett. **39**(7), 1996-1999 (2014).
14. P. Bon, G. Maucort, B. Watterllier, and S. Monnerret, "Quadriwave lateral shearing interferometry for quantitative phase microscopy of living cells," Opt. Express **17**(15), 13080-13094 (2009).
15. A. Barty, K. A. Nugent, D. Paganin, and A. Roberts, "Quantitative optical phase microscopy," Opt.Lett. **23**(11), 817-819 (1998).

16. C. Joo, T. Akkin, B. Cense, B. H. Park, and J. F. de Boer, "Spectral-domain optical coherence phase microscopy for quantitative phase-contrast imaging," Opt. Lett. **30**(16), 2131-2133 (2005).
17. E. Cuche, F. Bevilacqua, and C. Depeursinge, "Digital holography for quantitative phase-contrast imaging," Opt. Lett. **24**(5), 291-293 (1999).
18. C. J. Mann, L. F. Yu, C. M. Lo, and M. K. Kim. "High-resolution quantitative phase-contrast microscopy by digital holography," Optics Express **13**(22), 8693-8698 (2005).
19. B. Kemper, and G. von Bally, "Digital holographic microscopy for live cell applications and technical inspection," Appl. Opt., **47**(4), A52-A61 (2008).
20. D. Gabor, "A new microscopic principle," Nature **161**(4098), 777-778 (1948).
21. T. C. Poon, *Optical Scanning Holography with MATLAB*®. (Springer Science & Business Media, 2007).
22. J. W. Goodman, and R. W. Lawrence, "Digital image formation from electronically detected holograms," Appl. Phys. Lett., **11**(3), 77-79 (1967).
23. E. N. Leith, and J. Upatnieks, "Wavefront reconstruction with continuous-tone objects," JOSA **53**(12), 1377-1381 (1963).
24. U. Schnars, and W. Jüptner, "Direct recording of holograms by a CCD target and numerical reconstruction," Appl. Opt., **33**(2), 179-181 (1994).
25. I. Yamaguchi, and T. Zhang, "Phase-shifting digital holography," Opt. Lett., **22**(16) 1268-1270 (1997).
26. T. Kreis, "Digital holographic interference-phase measurement using the Fourier-transform method," JOSA A **3**(6), 847-855 (1986).
27. D. O. Hogenboom, C. A. DiMarzio, T. J. Gaudette, A. J. Devaney, and S. C. Lindberg, "Three-dimensional images generated by quadrature interferometry," Opt. Lett, **23**(10), 783-785 (1998)
28. G. Popescu, T. Ikeda, R. R. Dasari, and M. S. Feld, "Diffraction phase microscopy for quantifying cell structure and dynamics," Opt. Lett.,**31**(6), 775-777 (2006).
29. B. Bhaduri, H. Pham, M. Mir, and G. Popescu, "Diffraction phase microscopy with white light," Opt. Lett., **37**(6), 1094-1096 (2012).
30. T. Zimmermann, J. Rietdorf, and R. Pepperkok, "Spectral imaging and its applications in live cell microscopy," FEBS Lett. **546**(1), 87-92 (2003).

31. L. Barsback, J. Kopolovic, Z. Malik, and C. Rothmann, “Spectral morphometric characterization of breast carcinoma cells,” Br. J. Cancer **79**(9-10), 1613(1999).

32. G. J. Tearney, R. H. Webb, and B. E. Bouma, "Spectrally encoded confocal microscopy," Opt. Lett. **23**(15), 1152-1154 (1998).

33. L. Golan, D. Yeheskely-Hayon, L. Minai, and D. Yelin, "High-speed interferometric spectrally encoded flow cytometry." Opt. Lett. **37**(24), 5154-5156 (2012).

34. D. Yelin, W. M. White, J. T. Motz, S. H. Yun, B. E. Bouma and G. J. Tearney, "Spectral-domain spectrally-encoded endoscopy," Opt. Express **15**(5)**,** 2432-2444 (2007).

35. D. Yelin, B. E. Bouma, N. Iftimia, and G. J. Tearney, "Three-dimensional spectrally encoded imaging," Opt. Lett. **28**(23), 2321-2323 (2003).

Chapter 2

Theoretical Analysis and technical methods

In order to better understand the performance of the SMI system, the theoretical analysis of the incoherent optical system is necessary. Thus, the theorem of the incoherent optical system (especially 4F optical systems) will be discussed in this chapter. Besides, the major technical methods used in data processing will be demonstrated.

2.1 Theoretical analysis of the incoherent optical systems and SMI system using electromagnetic theorem and Fourier optics

The diffraction theorem is used to analyze the incoherent optical systems especially the 4F incoherent optical systems. Besides, the basic theoretical analysis of SMI system is demonstrated here.

2.1.1 Diffraction theorem in coherent and incoherent optical system

Since all the optical imaging process can be described and calculated by diffraction theorem, here, the diffraction theorem is used to analyze the principles of SMI. Firstly, the diffraction theorem in coherent and incoherent optical system is introduced and some simulations have been made.

As is known, Fresnel diffraction is often used to describe the light propagation in free space. The result will be a convolution between the original field with a spatial impulse response in Fourier Optics [1]. In 3D rectangular coordinate system, the expression is,

$$\varphi_p(x,y;z)=\frac{jk_0}{2\pi z}e^{-jk_0 z}e^{-j\frac{k_0}{2z}(x^2+y^2)}\tilde{F}\{\varphi_{p0}(x,y)e^{-j\frac{k_0}{2z}(x^2+y^2)}\}\Big|_{\substack{k_x=\frac{k_0 x}{z}\\ k_y=\frac{k_0 y}{z}}} \tag{2-1}$$

where $\varphi_{p0}(x,y)$ is the original field and $\varphi_p(x,y;z)$ is the field after propagating a distance of z.

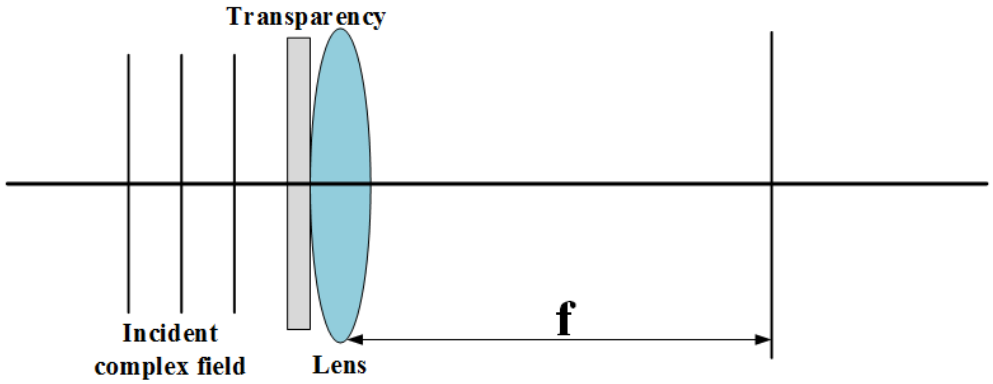

Fig. 2-1 Single lens optical system with transparent object very close to the lens

Specifically, for the optical system in Fig. 2-1, the field at the back focal plane of the convex lens will be,

$$\begin{aligned}\varphi_p(x,y;f) &= \frac{jk_0}{2\pi f}e^{-jk_0 f}e^{-j\frac{k_0}{2f}(x^2+y^2)}\tilde{F}\{t_f(x,y)e^{-j\frac{k_0}{2f}(x^2+y^2)}\}\Big|_{\substack{k_x=\frac{k_0 x}{f}\\ k_y=\frac{k_0 y}{f}}} \\ &= \frac{jk_0}{2\pi f}e^{-jk_0 f}e^{-j\frac{k_0}{2f}(x^2+y^2)}\tilde{F}\{e^{j\frac{k_0}{2f}(x^2+y^2)}e^{-j\frac{k_0}{2f}(x^2+y^2)}\}\Big|_{\substack{k_x=\frac{k_0 x}{f}\\ k_y=\frac{k_0 y}{f}}} \\ &\propto \quad \delta(\frac{k_0 x}{f},\frac{k_0 y}{f})\end{aligned} \tag{2-2}$$

where $t_f(x,y)$ is the transparency function of the lens. It means that the parallel beam after a convex lens will be focused, which is consistent with the ray theorem.

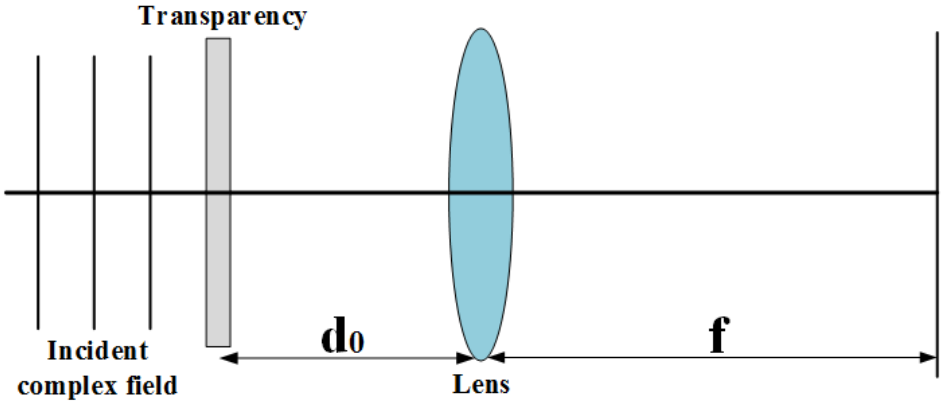

Fig. 2-2 Single lens optical system with transparent object a distance of d_0 in front of the lens

Further, if the transparent object is put at a distance d_0 in front of the lens as is shown in Fig. 2-2, the field at the back focal plane of the lens is,

$$\begin{aligned}\varphi_p(x,y;f) &= \{[t(x,y)*h(x,y,d_0)]t_f(x,y)\}*h(x,y,f) \\ &= \frac{jk_0}{2\pi f}e^{-jk_0 f}e^{-j\frac{k_0}{2f}(x^2+y^2)}\tilde{F}\{\tilde{F}^{-1}\{T(k_x,k_y)e^{-jk_0 d_0}e^{j\frac{k_0}{2d_0}(x^2+y^2)}\}\}\Big|_{\substack{k_x=\frac{k_0 x}{f}\\ k_y=\frac{k_0 y}{f}}} \\ &= \frac{jk_0}{2\pi f}e^{-jk_0(f+d_0)}e^{-j\frac{k_0}{2f}(1-\frac{d_0}{f})(x^2+y^2)}T(\frac{k_0 x}{f},\frac{k_0 y}{f})\end{aligned} \tag{2-3}$$

where $T(k_x,k_y)$ is the Fourier transform function of the object transparency function $t(x,y)$. We can see that if d_0=f, the final field is proportional to the Fourier transform of the object transparency function. The imaging plane is actually the so-called Fourier plane in optical systems.

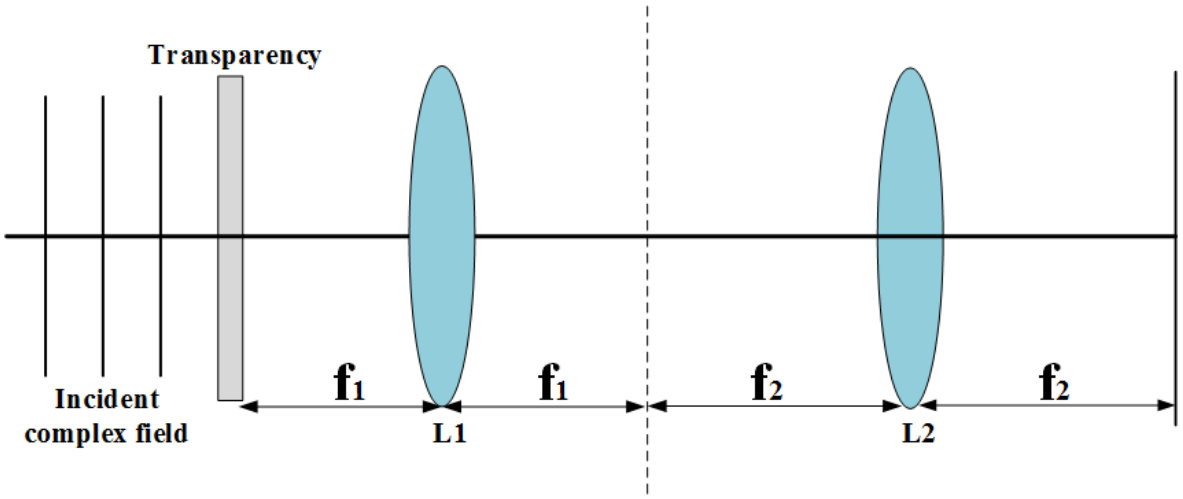

Fig. 2-3 A typical 4F system

Then, for a 4F optical system used in SMI as is shown in Fig. 2-3, applying the previous theorem, the field at the Fourier plane will be proportional to $T(k_x,k_y)$. After passing the pupil and another lens, the final field at the image plane is,

$$\begin{aligned}\varphi_{pi}(x,y) &\propto \tilde{F}\{T(\frac{k_0 x}{f_1},\frac{k_0 y}{f_1})p(x,y)\}\Big|_{\substack{k_x=\frac{k_0 x}{f_2}\\ k_y=\frac{k_0 y}{f_2}}} \\ &\propto t(\frac{x}{M},\frac{y}{M})*\tilde{P}(\frac{k_0 x}{f_2},\frac{k_0 y}{f_2})\end{aligned} \tag{2-4}$$

where M is the ratio of f_2 and f_1; $\tilde{P}(\frac{k_0 x}{f_2}, \frac{k_0 y}{f_2})$ is the Fourier transform of the pupil function, which is also called the point spread function (PSF). If the pupil function is 1, the field at the image plane will be proportional to the magnified/compressed version of the object transparency function. This is why we would like to introduce 4F optical systems in SMI system. By introducing 4F optical systems, the image at the image plane will be static without influence from galvo scanning, so that the beam will always fully fill the aperture of the objectives.

The above theorem is eligible for coherent optical systems. In incoherent optical systems, the intensity of the object is used for convolution with the system's point spread function rather than the amplitude. Therefore, the acquired intensity distribution at the image plane will be,

$$I_i \quad \propto \quad \left| t(\frac{x}{M}, \frac{y}{M}) \right|^2 * \left| h_c(x, y) \right|^2 \tag{2-5}$$

where $|h_c(x,y)|^2$ is the intensity PSF. The Fourier transform for the intensity PSF is called the optical transfer function (OTF). We can find that the OTF corresponds to an auto-correlation so that it is always a low-pass filter.

2.1.2 Simulations in incoherent optical systems

Here are some simulations about the incoherent optical system. Suppose the object is a slit shown in Fig. 2-4 (a). Fig. 2-4 (b) shows it Fourier transform.

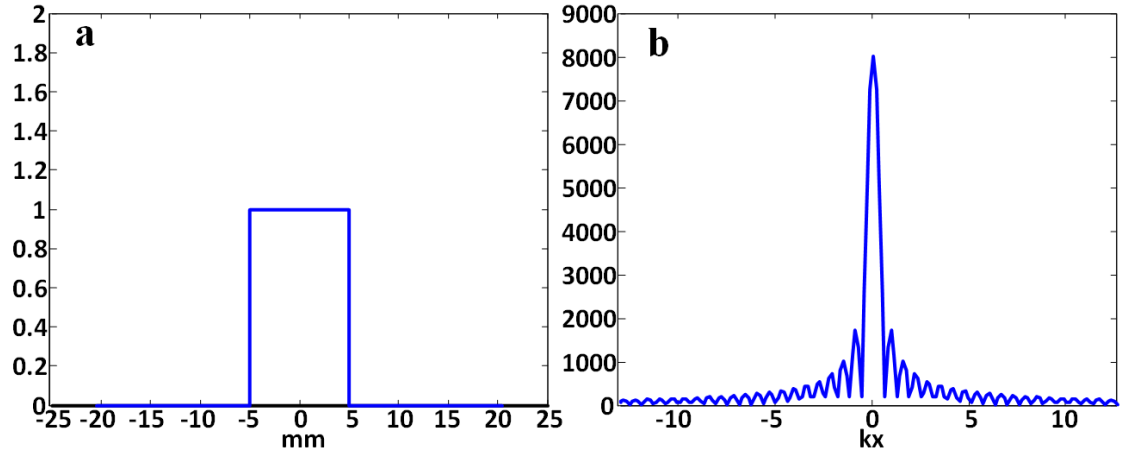

Fig. 2-4 (a) Slit object for simulation; (b) Corresponding Fourier transform of (a).

Fig. 2-5 shows the pupil function and its corresponding OTF for the incoherent optical system.

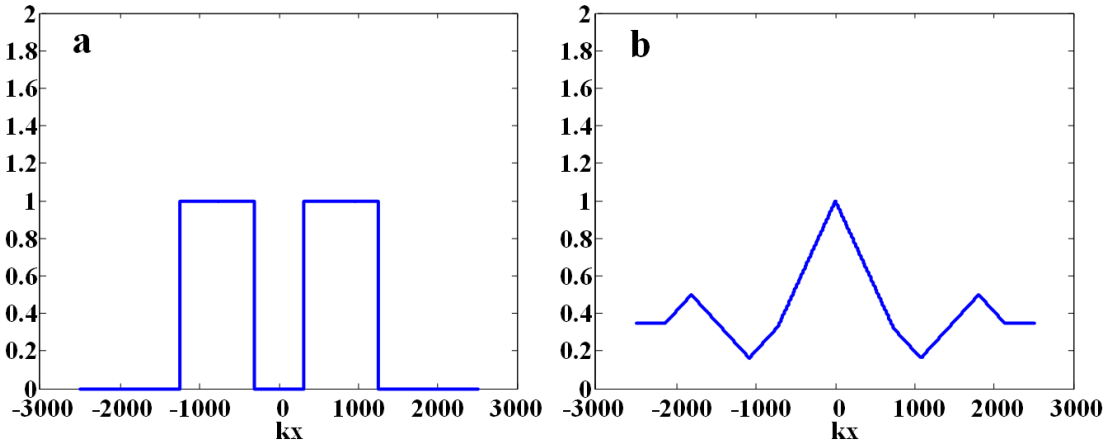

Fig. 2-5 (a) Pupil function; (b) Corresponding OTF in incoherent optical system.

The final processed image is shown in Fig. 2-6,

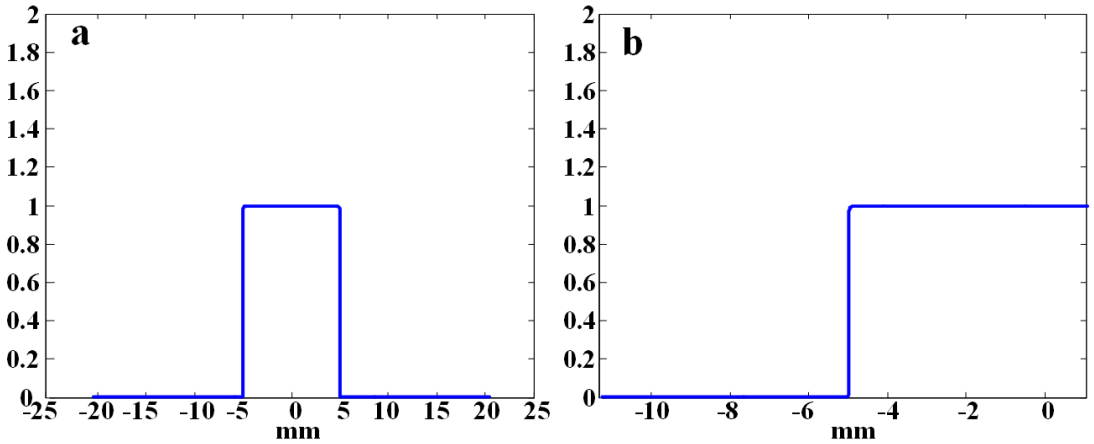

Fig. 2-6 (a) Final processed image; (b) Amplified edge in (a).

We can see that after incoherent 4F optical system, the image at the image plane is almost the same as the object except a little blurred edge.

2.1.3 Basic analysis of SMI system

SMI is actually a confocal optical system [2,3]. To analyze the SMI system, we need firstly to analyze the image formation of confocal optical systems. Fig.2-7 shows a typical configuration of the confocal optical system.

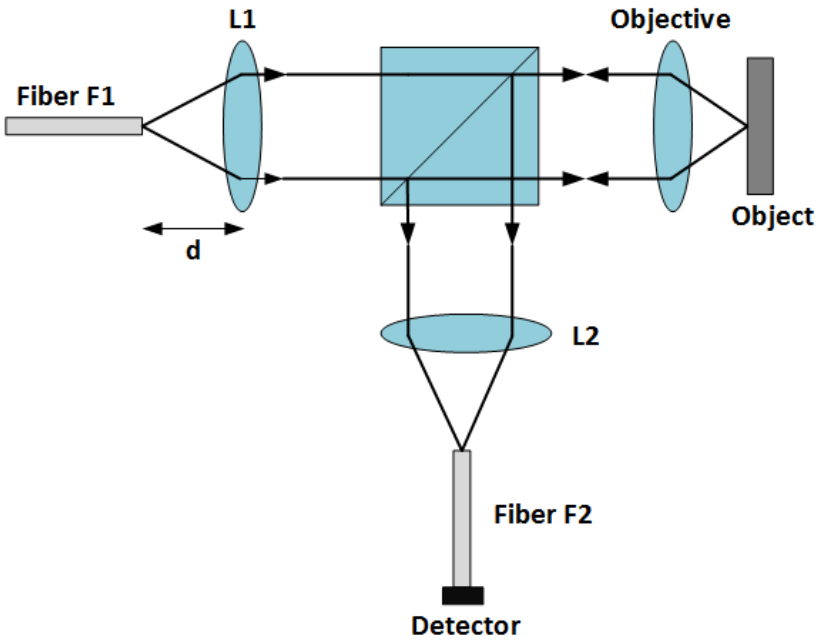

Fig.2-7 A typical configuration of the confocal optical system

According to the imaging theorem, the field amplitude at a point x_2 on the input end of the fiber F_2 with respect to the reflection point x_s is,

$$U_2(x_s, x_2) = \int_{-\infty}^{\infty} U_1(x_0) h_1(x_0 + \frac{x_1}{M_1}) r_f(x_s - x_1) h_2(x_1 + \frac{x_2}{M_2}) dx_0 dx_1 \tag{2-6}$$

where $U_1(x_0)$ is the amplitude of distribution of the field at the output end of the optical fiber F_1, h_1 and h_2 are the amplitude PSF, corresponding to the Fourier transform of the pupil functions. M_1 and M_2 are the magnification of the lens respectively. After considering the field transmission inside the single-mode fiber, the intensity distribution at the output end of the fiber F_2 is,

$$\begin{aligned} I(x_s) = \int\int\int\int\int\int_{-\infty}^{\infty} & f_1^*(x_2) U_1(x_0) h_1(x_0 + \frac{x_1}{M_1}) r_f(x_s - x_1) h_2(x_1 + \frac{x_2}{M_2}) f_1^*(x_2') U_1^*(x_0') \\ & \times h_1^*(x_0' + \frac{x_1'}{M_1}) r_f^*(x_s - x_1') h_2^*(x_1' + \frac{x_2'}{M_2}) dx_0 dx_0' dx_1 dx_1' dx_2 dx_2' \end{aligned} \tag{2-7}$$

where $f_1(x)$ is the field distribution of the single-mode fiber. Then we can derive the final intensity distribution from Eq. (2-7) as,

$$I(x_s) = \left| h_{eff}(x_s) \otimes r_f(x_s) \right|^2$$
$$h_{eff}(x) = (U_1(\frac{x}{M_1}) \otimes h_1(\frac{x}{M_1}))(f_1^*(\frac{x}{M_1}) \otimes h_2(x)) \quad (2\text{-}8)$$

Eq. (2-8) shows that the confocal optical system is actually a coherent system with an effective PSF.

With the basic knowledge of confocal optical system, we can analyze the SMI system. For the SMI system, within the optical system, due to the 4F systems, when reflecting back, the optical system does not change the interference information but only a matter of magnification. With coupling back into the optical fiber, as is analyzed in confocal optical system, the output field is actually the convolution of the reflected field from the optical system with the effective PSF. Suppose the complex reference and sample fields after the optical fiber can be written as $U_r = E_r \exp[j2k(y)L_r]$ and $U_s(x,y) = E_s(x,y)\exp[j(2k(y)L_s + 2\phi_s(x,y))]$, where L_r and L_s are sample arm and reference arm pathlength of the interferometer, and the corresponding phase depends on spatially dispersed wavenumber, $k(y)$, which can be written as $k(y) = k_0 + \alpha y$ with k_0 being the staring wavenumber and α being the dispersion coefficient. The dispersion coefficient is proportional to the magnification of the 4F system after the grating and inverse proportional to the angular dispersion coefficient of the grating and the focal length of the objective. Suppose that $L_0 = L_s - L_r$, which is the pathlength difference of the two arms, the total detected interference intensity hence is,

$$I_{tot}(x,y) = \left|E_r\right|^2 + \left|E_s(x,y)\right|^2 + 2E_rE_s(x,y)\cos(2k_0L_0 + 2\alpha yL_0 + 2\phi_s(x,y)) \quad (2\text{-}9)$$

Therefore, the final original interference image we acquire from the CCD camera is,

$$I_{final} = \int h_{SPM}^2 \otimes I_{tot}(x,y) \quad (2\text{-}10)$$

where h_{SPM} is the PSF of the optical system in spectrometer. Thus, the spectral-domain filter for the interference signal will be like the shape in Fig. 2-8.

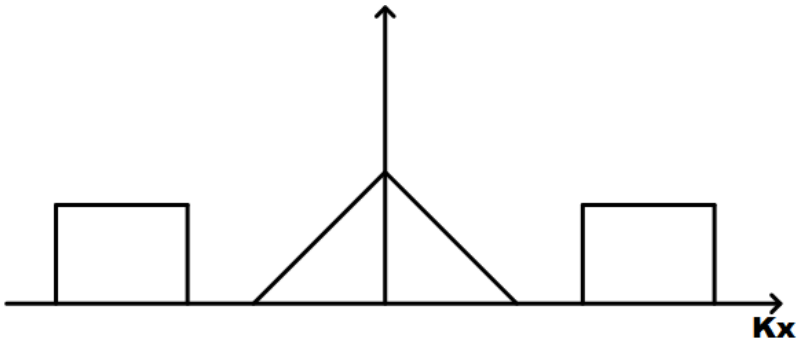

Fig. 2-8 Corresponding spectral filter in SMI system

Usually, the width of the central part of the filter will be 2 times that of the left and right side part. However, due to the effect of coupling back into the fiber, the ratio will be a little lower than 2. It is consistent with our experimental results when looking at the spectral domain of the interference signal in Fig. 3-4 (b).

2.2 Goldstein 2D phase unwrapping

In order to get the quantitative phase image, phase information must be extracted from the modulated signal during the signal processing. However, the demodulated phase might not be continuous as expected even though the optical phase is softly increasing or decreasing. The discontinuous phase usually happens when extreme phase values + π or -π is reached, which makes a 2π phase jump to happen in the neighboring two points.

Fig. 2-9 (a) shows the expected phase linearly proportional to the measured physical parameter such as thickness, displacement, etc. However, when demodulating the modulated signals (usually interference signals in optics), the range of the demodulated phase will be limited from – π to + π. Any phase value beyond this range will be suppressed back to this range as shown in Fig. 2-9 (b). In order to extract the original continuous phase information, integral multiples of 2π need to be added or subtracted on the phase jump points. The operation that determines the order of each fringe and restore the continuous phase map is called the phase unwrapping. Since, the acquired image from our SMI system is two dimensional, the 2D phase unwrapping is one important procedure in the signal processing.

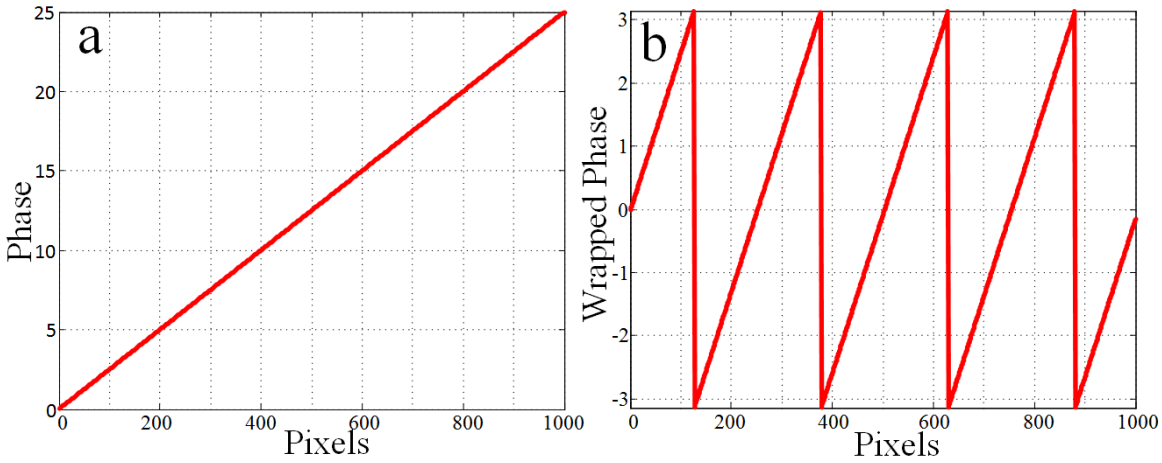

Fig. 2-9 (a) Expected continuous phase; (b) Demodulated wrapped phase.

The algorithm of phase unwrapping can be classified into two categories:

(1) Global algorithm: independent of the path followed on the phase map. It follows only one step to identify, isolate and exclude the locations of the phase difference that leads to an error when discontinuity occurs. This phase unwrapping process follows an arbitrary path;

(2) Local algorithm: dependent on the path, giving the continuous phase by following the given path.

For our signal processing, Goldstein's algorithm [4,5], a path-dependent method, is used for phase unwrapping. Ideally, if we generate a looped path on any region of the ideal phase image, the sum of the phase difference between each adjacent pixels should be 0. However, due to the noise and the phase jump, this sum sometimes will not be 0. Then, the pixel will be labeled as a residue. The path that connects the two opposite residues is called the branch cut. Goldstein's algorithm develops a method to detect residues and connect the residues with branch cuts. The procedure is as the following [4],

Firstly, a residue should be found by scanning. Once a residue is found, a box of size 3 will be placed around the residue and try to find another residue. If another residue is found and is of opposite sign to the original residue, a branch cut will be placed between them and be designated as 'uncharged'. Then, we continue to find another residue. If the sign of the residue is the same as the original residue, the box will be placed around this new residue and search for other residues until an opposite residue is found.

This is a brief description of this Goldstein's algorithm. Many specific steps need to be performed.

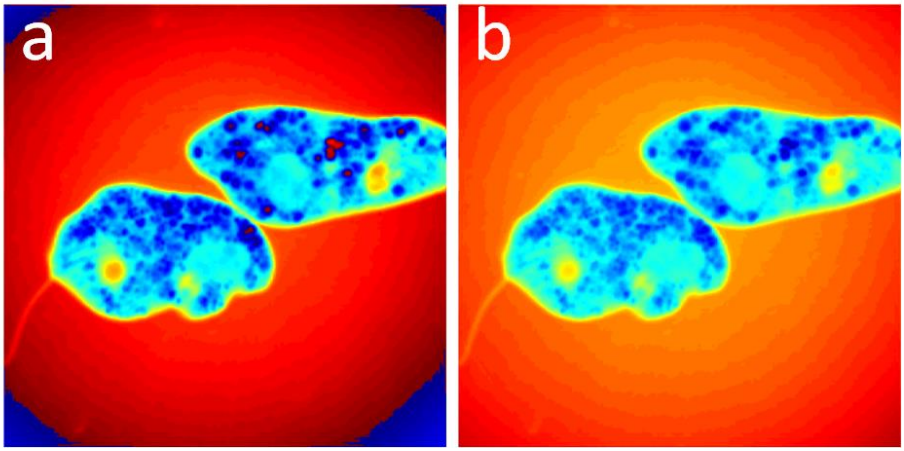

Fig. 2-10 (a) Wrapped phase image of Peranema; (b) Unwrapped phase image of Peranema using Goldstein's phase unwrapping algorithm.

Fig. 2-10 (a) shows the 2D wrapped phase image. It is clearly seen that there are phase jumps at some positions. Fig. 2-10 (b) shows the 2D unwrapped phase image from Goldstein's algorithm. The phase jump has been corrected to form continuous phase.

2.3 Zernike polynomial background subtraction

Because of the optical aberration and non-optimal correction existing in the SMI system, even after the phase unwrapping and phase-to-OPL conversion, there will still be a background together with the designated OPL distribution Therefore, the Zernike polynomial fitting [6] is applied to the demodulated image after phase unwrapping for background subtraction. Briefly, according to the analysis of the aberrations and diffraction, a set of orthogonal polynomials with unit disk are used to describe the aberrations and diffraction. There are even and odd Zernike polynomials as shown in Eq. (2-11),

$$\begin{aligned} Z_n^m(\rho,\varphi) &= R_n^m(\rho)\cos(m\varphi) \quad (even) \\ Z_n^{-m}(\rho,\varphi) &= R_n^m(\rho)\sin(m\varphi) \quad (odd) \end{aligned} \tag{2-11}$$

where the radial part is defined in Eq. (2-12),

$$R_n^m(\rho)=\sum_{k=0}^{\frac{n-m}{2}}\frac{(-1)^k(n-k)!}{k!(\frac{n+m}{2}-k)!(\frac{n-m}{2}-k)!}\rho^{n-2k}\qquad 0\le\rho\le 1 \tag{2-12}$$

With these orthogonal polynomial bases, we can use the weighted combination of them to fit the background and remove it from the demodulated OPL image.

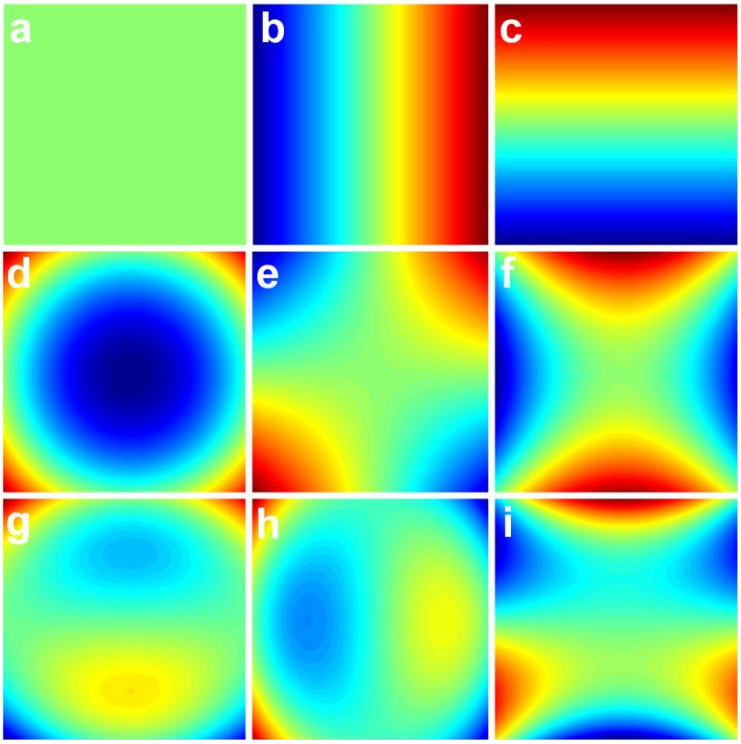

Fig. 2-11 The first nine sets of the Zernike polynomial orthogonal bases

Fig. 2-11 shows the first nine orders of the Zernike polynomials. According to the experiment, for most of the time, the first eight orders of the polynomials are enough to fit the background within the tolerant errors.

In order to use the Zernike polynomial fitting for background subtraction, we need to give a corresponding mask to determine whether each point on the image is a background point or not. In our signal processing program, we use two standards to select the background points and do Zernike polynomial fitting for two times according to the two masks.

The first mask is made according to the threshold with respect to the gradients of the data [6] according to Eq. (2-13),

$$\sqrt{\frac{\partial^2 \varphi}{\partial x^2} + \frac{\partial^2 \varphi}{\partial y^2}} \tag{2-13}$$

The assumption is made that the gradient values of the data at the maximum occurrence will be related to the background. Therefore, the process of generating the mask according to the gradients of the data is as the following:

(1) Calculate the gradient values of the image data;

(2) Generate an interface to show the corresponding mask with respect to the gradient threshold. Adjust the threshold until the corresponding mask is satisfied. Save the mask in the file.

(3) Use the generated mask together with the original data to calculate the Zernike background surface from the non-masked pixels.

(4) Subtract the fitting background from the original image to get the pure OPL image of the sample.

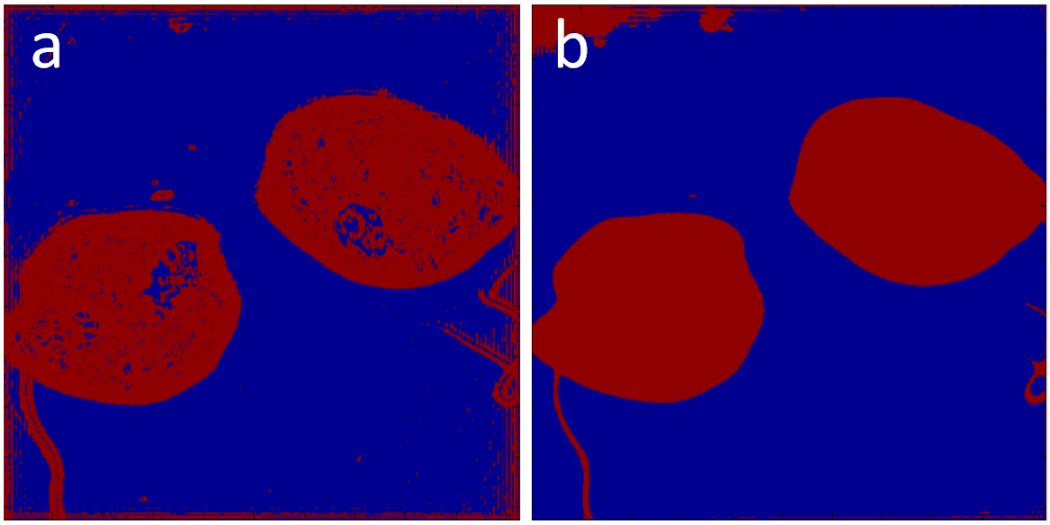

Fig. 2-12 Two types of masks for Zernike Polynomial background subtraction; (a) gradient mask; (b) intensity mask;

Fig. 2-12 (a) shows a typical mask based on the gradient values of the given OPL image. We can see that most parts of the objects in the image have been selected. Then, the non-masked pixels will be regarded as background for Zernike polynomial background subtraction.

However, only based on the gradient standard to generate the mask for background subtraction may not be absolutely accurate to separate the objects and the background. As is seen in Fig. 2-

12 (a), there are still some pixels on the objects being regarded as background pixels. Therefore, another standard of generating the mask is introduced for the second-time background subtraction. After the first-time background subtraction, the background is almost flat so that the intensity can be used as a ruler to separate objects and background. The intensity will be around 0 for the background and will be a much higher (or lower) value for the object. Fig. 2-12 (b) shows the mask based on the intensity of the image. We can see that all parts of the objects have been regarded as the masked pixel. Similarly to the first-time background subtraction, the procedures of the second-time background subtraction are shown as the following:

(1) Loading the image after the first-time background subtraction;

(2) Generating an interface to show the corresponding mask with respect to the intensity threshold which can be adjusted in the interface. All the pixels above the threshold will be masked. Adjust the intensity threshold until it is satisfied. Save the mask in the file;

(3) Use the generated mask with the given image to calculate the Zernike background surface with the non-masked pixels in the mask;

(4) Subtract the second-time background from the given image to further improve the quality of the image.

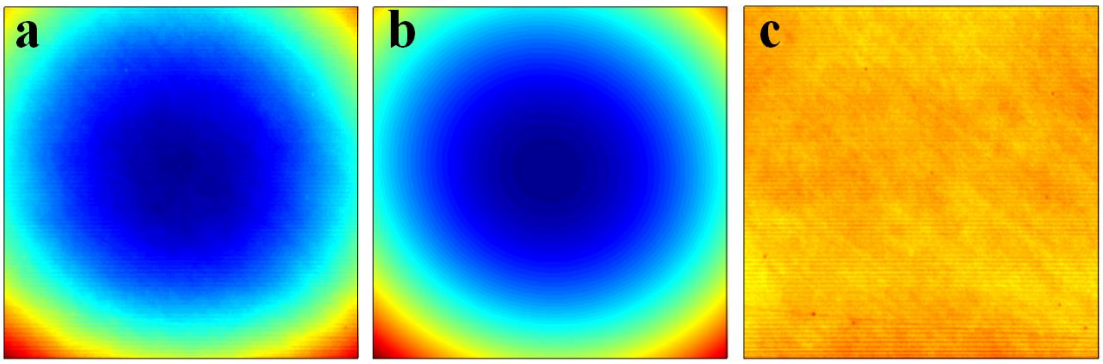

Fig. 2-13 The Zernike polynomial process for background subtraction using gold mirror; (a) original OPL image with background; (b) fitting background using Zernike polynomials; (c) OPL image after background subtraction.

To show the performance of the Zernike polynomial background subtraction, a gold mirror was used as the sample. Fig. 2-13 (a) shows the original OPL image with background added on it. Fig. 2-13 (b) shows the fitted background using Zernike polynomial with the first eight

orthogonal polynomial bases. Fig. 2-13 (c) shows the final OPL image of the gold mirror surface. The scratched line on the gold mirror can be clearly detected, which shows that the Zernike polynomial has a good performance for background subtraction.

2.4 References

1. T. C. Poon, *Optical Scanning Holography with MATLAB®*. (Springer Science & Business Media, 2007).
2. S. Kimura, and T. Wilson, "Confocal scanning optical microscope using single-mode fiber for signal detection," Applied optics **30**(16), 2143-2150 (1991).
3. M. Gu, C. J. R. Sheppard, and X. Gan, "Image formation in a fiber-optical confocal scanning microscope," JOSA A **8**(11), 1755-1761 (1991).
4. D. C. Ghiglia, and M. D. Pritt, *Two-dimensional phase unwrapping: theory, algorithms, and software*. (New York:: Wiley, 1998).
5. R. M. Goldstein, H. A. Zebker, and C. L. Werner, "Satellite radar interferometry: Two dimensional phase unwrapping," Radio Science **23**(4), 713-720 (1998).
6. K. Creath and G. Goldstein, "Dynamic quantitative phase imaging for biological objects using a pixelated phase mask," Biomed. Opt. Express **3**(11), 2866-2880 (2012).

Chapter 3

System description and experimental results

In this chapter, firstly, the optical setup of the SMI system is introduced in detail. Secondly, the corresponding Labview program to control the system and the Matlab program for signal processing are described with flow diagrams. Then, the quantitative phase imaging of the reflection object-USAF resolution target using SMI system is demonstrated. The comparison of the height measurement with other commercial devices is made and its temporal and spatial sensitivity is quantitatively demonstrated. After that, several biological samples (dynamic and static) are used to test the performance of the SMI system when measurement transparent biological samples. The experimental results confirm that the SMI has the advantages of speckle-free, high resolution, high sensitivity while maintaining high image acquisition rate. Higher sensitivity with higher image acquisition rate can be achieved with system optimization.

3.1 System and programs

The SMI system will be demonstrated in detail in this part. Besides, the Labview and Matlab programs to control the system and process the acquired data are discussed here respectively.

3.1.1 Description of the SMI system

Figure 3-1 shows the implementation of the SMI system. The input light is from a broadband singlemode superluminescent diode (SLD, Superlum; λ=837nm, $\Delta\lambda$=54nm). The input light is then coupled through a 50/50 fiber-optic coupler into the system. An optical circulator could also be used instead of the fiber-optic coupler to achieve higher input intensity. Then, a collimating package is put in front of the output of the fiber-optic coupler to generate a parallel light beam. After collimating package, the light will pass through a 1D galvanometer scanner to achieve scanning along x direction. Imaging from another direction (y direction) is achieved by light dispersion with a transmission grating (Wasatch Photonics; 600 l/mm). A 50:50 beam splitter is used to separate the light beam to the sample arm and reference arm, respectively. Two identical

objectives (Carl Zeiss; 40×, 0.65) are used to focus the light on the sample and the reference mirror, forming a line illumination [1,2] at each galvanometer scanning position. With two identical objectives, the wave front difference will be eliminated. Besides, two 4F systems are incorporated in the SMI system for magnification. From the theorem in chapter 2, we know that the 4F system does not affect the relation of object and image.

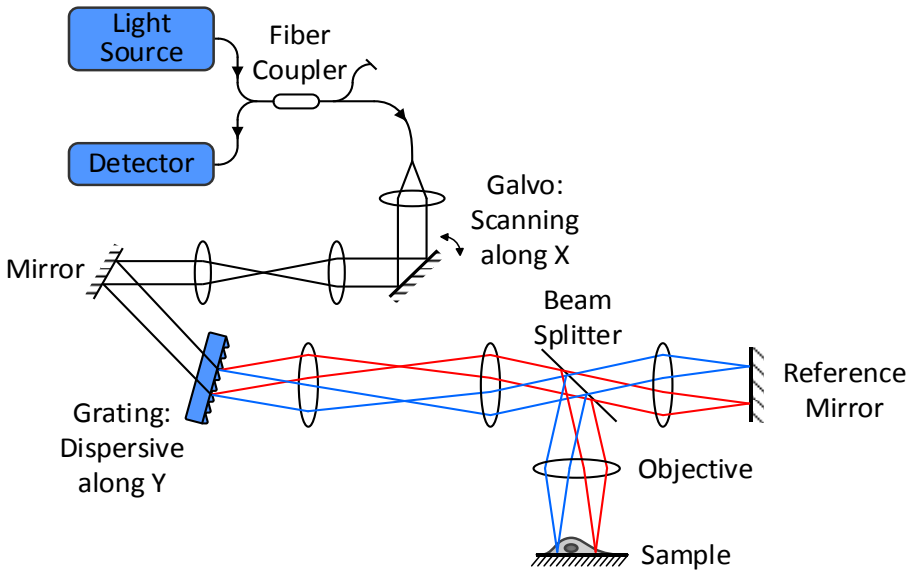

Fig.3-1 Schematic of the SMI system [3] R. B. Shang, S. C. Chen, C.S. Li, and Y. Z. Zhu, "Spectral modulation interferometry for quantitative phase imaging," Biomedical Optics Express **6**(2), 473-479 (2015). Used under fair use, 2015.

For transparent biological samples such as living cells, they will be put on a reflected surface (a gold mirror in our experiment). The light will pass through the transparent biological samples back and forth, generating two-times pathlength difference with respect to the reference arm. For non-transmitted object such as the resolution target measured in the experiment, the light will just reflected from the surface and no reflected surface is needed under the object. For transparent biological samples, since penetrating through the samples will result in energy loss of the light beam, a different transmission-reflection ratio beam splitter could be used to enhance the energy of the light beam to the sample arm to better balance the energy of the light beams reflected from the two arms.

The reflected light carrying the sample information will be coupled back to the optical fiber coupler and received by the detector (spectrometer). In order to prevent the light being coupled

back to do damage to the light source, an isolator should be applied to prevent backward light. Within the detector, a CCD camera (e2v; EM1, 1024 pixel, highest line rate 78 kHz) is used to receive the light and to send the electronic signal to the computer for future processing. The camera exposure time is set as 12 usec (shortest allowed exposure time) for all different scanning rates. The total waveform is called Raster cycloidal waveform. The linear portion in the middle is the normal working period for the galvanometer. Between the connections of two linear portion, there is a fly-back part for the galvanometer to return to the original position with fast and smooth transition.

The camera is triggered for signal acquisition when the trigger of the galvanometer is in the linear portion of the forward scanning period. After successively getting a number of lines of the signal set in Labview, the camera will package the data together and send it to the computer as a 2D data, representing the 2D original interference image. There are two ways of increasing the image acquisition rate. One is to reduce the duration of the linear forward scanning period. Another one is to reduce the pixel numbers along scanning direction. This is why for 66.9 Hz frame rate, we get the image with 1024×1024 pixels and for 120.6 Hz frame rate, we only get the image with 1024×512 pixels.

3.1.2 Labview program to control the system

To control the whole optical system, the Labview programming is applied to integrate the DI card (National Instrument), galvanometer and the CCD camera. Firstly, the galvanometer need to be calibrated so that we can know the ratio between the final field of view scanning on the sample and the voltage added to the galvanometer. This value is a constant in the program as long as the system is not changed. Then, the Labview program will calculate some related parameters such as the frame rate, galvo voltage, etc. according to the input parameters (field of view, pixels numbers along scanning direction, etc.). For most of the time, we will adjust the position of the sample, find the right focused place without obtaining the data. Thus, a slow-scanning mode is created in the Labview program. For slow-scanning mode, the full speed trigger period is set as 100 microseconds so that the linear-forward portion of the galvanometer movement will be longer. This will make the galvanometer not to move back and forth so fast during the sample adjustment period to prevent over-thermal effects. When we want to start

scanning the sample and get the corresponding data, we will choose to let the program enter the fast-scanning mode. This time, the full speed trigger period will be set as 13 microseconds (shortest achievable trigger period of the system). In this case, the galvanometer will move back and forth according to the designed Raster cycloidal waveform at the fastest achievable rate. After getting and saving the data into the computer, the program will return to the slow-scanning mode for future adjustment. For the current system, the fastest achievable speed is 120.6fps with 1024×512 pixels for each image. Fig. 3-2 shows the flow diagram of the Labview program to control the system.

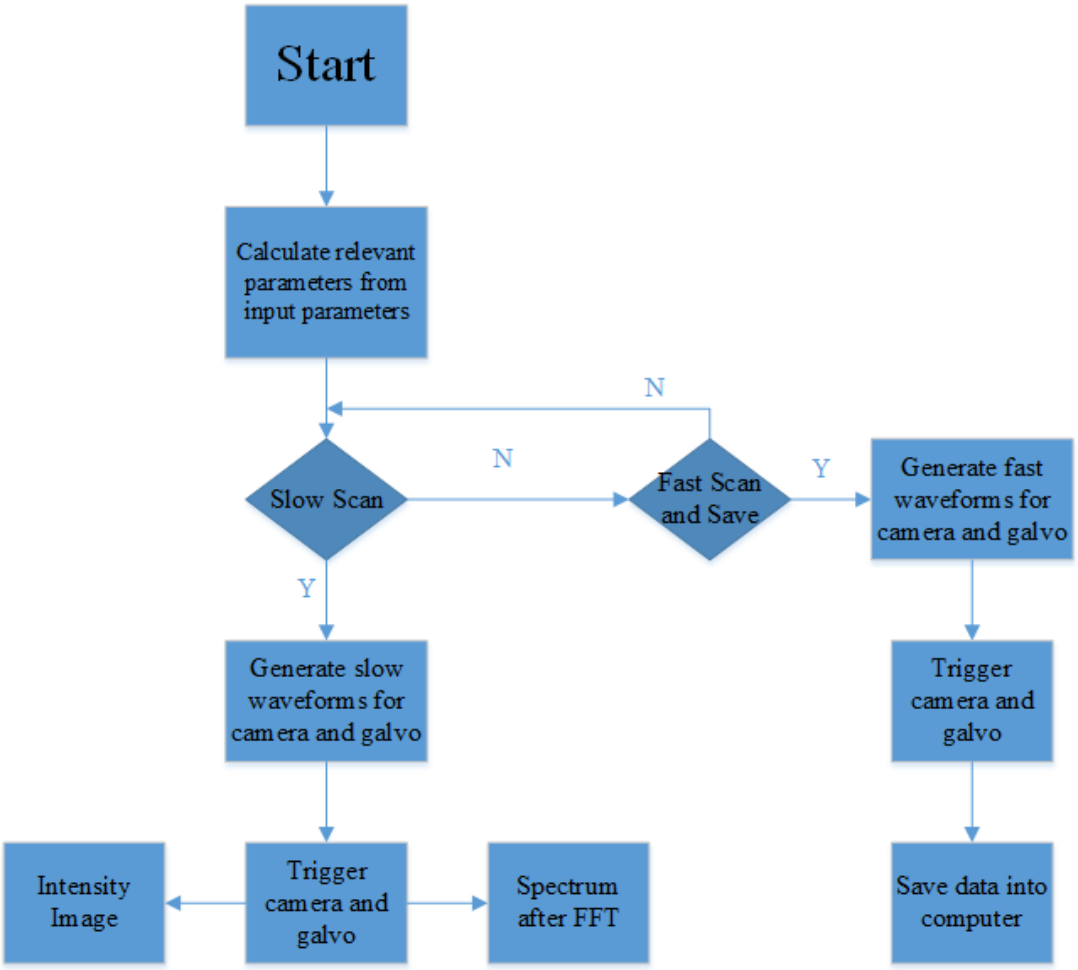

Fig. 3-2 Flow diagram of the Labview program

3.1.3 Matlab program for image processing

Matlab is used for image processing with the acquired data from the CCD camera. Fig. 3-3 shows the flow diagram of the whole image processing procedures in Matlab programs. Some other Matlab programs are also included to plot the final image and make the dynamic videos.

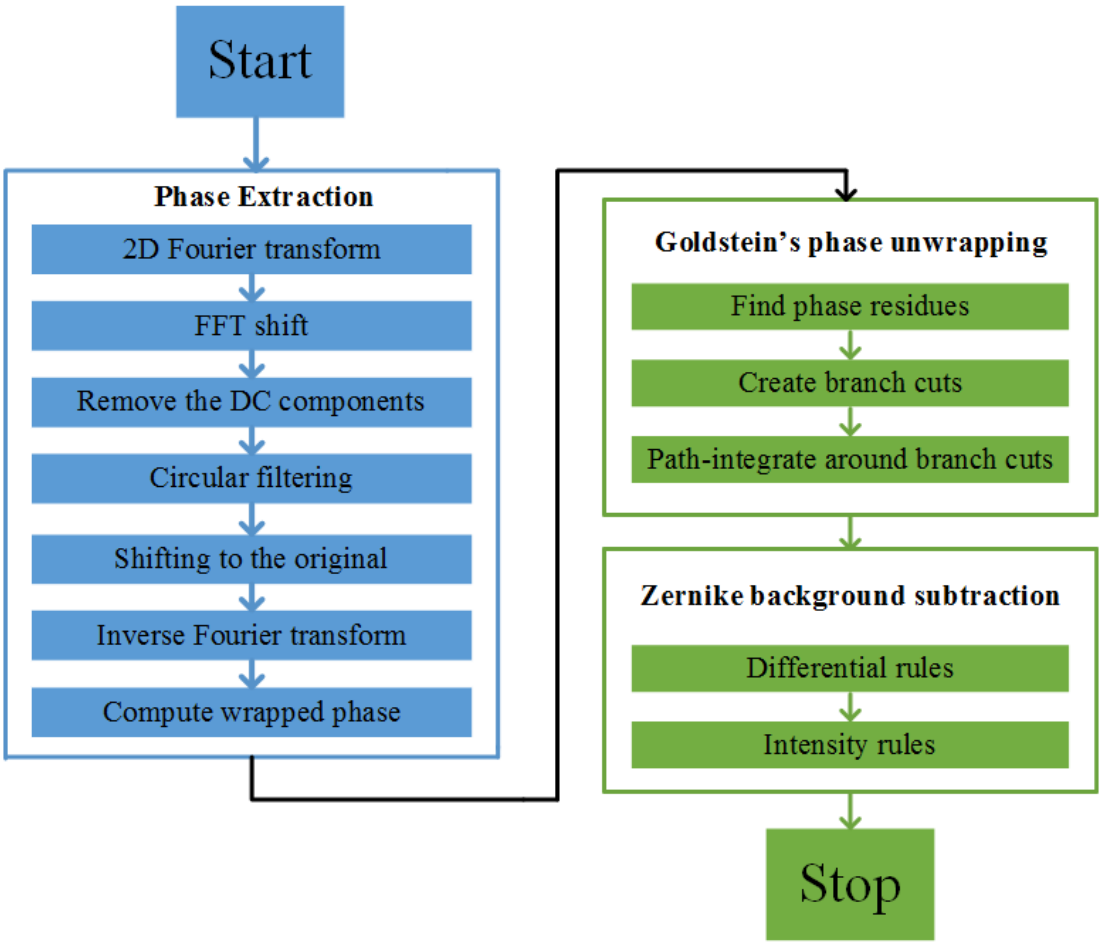

Fig. 3-3 Flow diagram of the data processing procedure in Matlab programs

The idea of SMI technique is similar to the digital holography. Thus, the data processing method is also similar to that of the digital holography [4-7]. Since low coherence light is used in SMI system instead of lasers, the uneven distributed wavenumber sampling of the original data should be resampled to the linear wavenumber sampling for future processing. Since the sampling density is high in SMI system, a sinc interpolation method is used to make the resampling within tolerant errors.

Then, a 2D Fourier transform is applied to the modified data after interpolation. In Fourier domain, with the carrier frequency from the pathlength difference of the two arms, the useful

signal will be moved to the high frequency region while the DC components will remain in the low frequency region. In this case, the useful signal can be seperated from DC components as long as a proper carrier frequency is selected. How to select the carrier frequency is an important factor to the success of the experiments. Different samples have different range of the frequency components in Fourier domain. For instance, the biological samples will usually have more frequency components in Fouier domain than that of the objects with regular shapes. It can be proved from our experiments that the frequency components of the biological samples Peranema and human-being cheek cells are more than that of the resolution target. Therefore, the carrier frequency added in the SMI system by means of adjusting the relative positions of the sample and reference arms is not a fixed number. It needs to be changed with different samples and may not be determined theoretically. Here, we just use experimental methods to determine the carrier frequency. For an unkonwn sample, we can get the original interference image from the system and do 2D Fourier transform in Matlab. There, we can know that if the useful signals with carrier frequency overlap with the DC components. If there is an overlap, we can increase the carrier frequency step by step until the useful signals with carrier frequency are totally separated from the DC components in Fourier domain.

After this, a circular band-pass filter is used to select the useful signal while the DC components and the conjugate part of the useful signal will be eliminated. How to determine the size of the circular filter and its shape is another important factor. Theoretically, the size of the circular filter can be calculated based on the system. However, because of the complexity of the system, the calculated size cannot be exactly accurate. In this case, most of the time, we will determine the size of the filter by looking at the boundary of the frequency components in Fourier domain. Besides, the shape of the filter is also of importance. For our current demodulation process, we only use the shape-edge circular filter. Sometimes, at the edge of the demodulated image, there will be a little ringing effect. However, since it does not affect the whole image a lot, we have not modified it. In the future, special-shaped circular filters in frequency domain such as Butterworse filter[8] might be used to reduce the ringing effect.

Then, an inverse Fourier transform is applied to it to change back to the time domain. Afterwards, the carrier frequency is removed to get the pure useful signal in time domain. Up to this step, the function ‘angle’ in Matlab is applied to compute the 2D wrapped phase. In order to get the continuous phase distribution, the Goldstein 2D phase unwrapping [9] as mentioned in

chapter 2 is applied to get the 2D unwrapped phase. Since we know the corresponding wavelength at each pixel position, we can calculate the optical pathlength at each pixel position. Using this method, we convert the 2D unwrapped phase distribution into 2D OPL distribution. Besides, due to the abberation issues in the optical system, the Zernike background polymonial subtraction method is applied to remove the background with differential judgement and intensity judgement. The details of its principles have been demonstrated in Chapter 2. With some other specific operations, the final 2D optical pathlength image will be acquired.

3.2 Quantitative phase image of the USAF resolution target and gold mirror from SMI system

In order to demonstrate the performance of the SMI technique, a 1951 USAF resolution target (Edmund Optics) is used to show the surface profile and the performance of the system. The sample bars on the resolution target are made from chromium. An $83.92 \times 83.92\ \mu m^2$ area of the resolution target is imaged containing Group 6, Element 1, in which the width of the bar is $7.81 \mu m$. The whole image contains 1024×1024 pixels. With these parameters, we can calculate that the average sampling interval of the spectral direction is 0.082 nm, which can guarantee that the modulated signal can be shifted far enough from DC components in Fourier domain to avoid overlaps. Theoretically, the minimum sampling frequency is determined by the sample's image bandwidth which is related to the point spread function of the optical system. However, since this point spread function is quite complicated with relation to the objectives used and the coupling optical fiber, we usually experimentally determine the sampling frequency by looking at the spectrum in Fourier domain. To adjust this sampling frequency, we can adjust the two sets of the 4F system. Since the carrier frequency shifted in the scanning direction needs to adjust the angle of the reference mirror, making it not perpendicular to the objective anymore, it will result in aberration issues and more energy loss. Therefore, only carrier frequency in spectrum direction is added. With the square field of view and the same pixel numbers in both directions, the sampling intervals in the scanning direction is the same as that of the spectral direction. However, this is not a requirement because no carrier frequency is added in the scanning direction as long as it satisfies the Nyquist-Shannon theorem. This is why for the 120.6 fps image, the size can be 1024×512 pixels still with the same field of view $83.92 \times 83.92\ \mu m^2$.

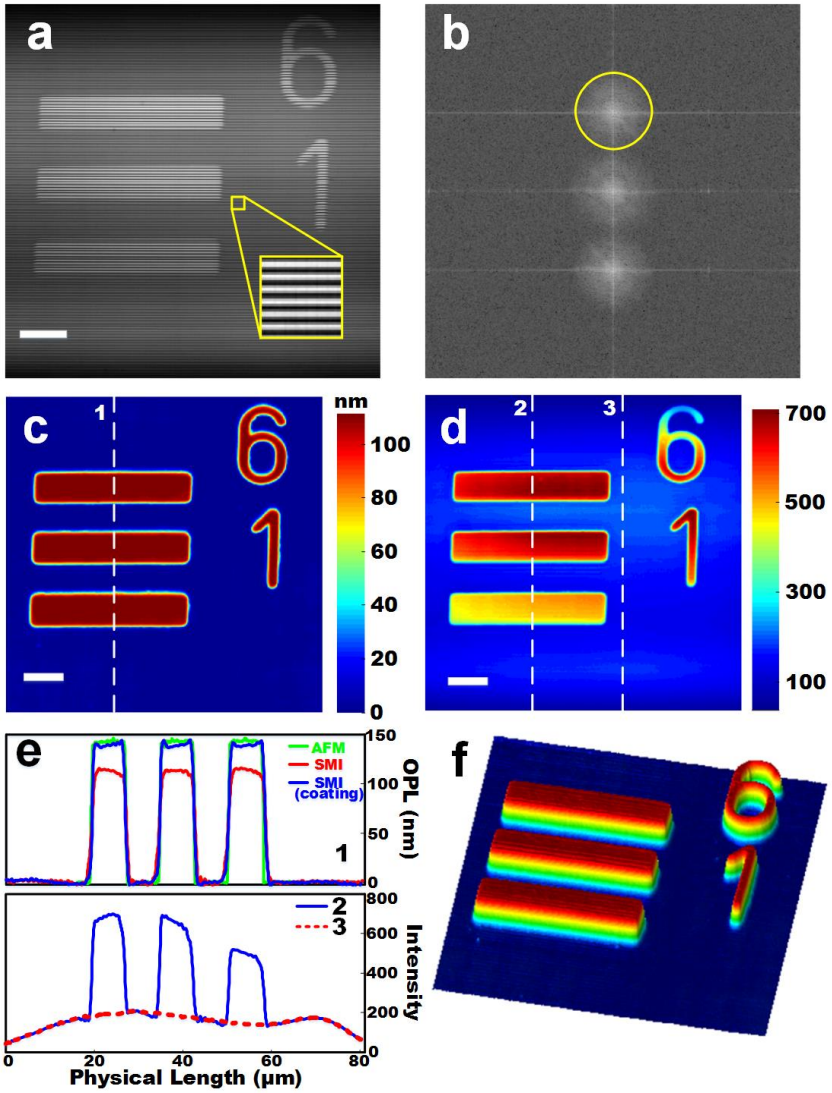

Fig. 3-4 Quantitative phase images of the resolution target from SMI system. (a) 2D original interferogram; (b) 2D FFT of the original interferogram in (a) with a circular filter for the designated signal; (c) 2D demodulated OPL image of the resolution target; (d) 2D demodulated intensity image of the resolution target; (e) 1D cross-sectional profiles of the curve marked as dash lines in (c) and (d); The upper image also includes the OPL measurement from AFM and SMI after Ag coating on the resolution target; (f) 3D OPL image of the resolution target. Bar represents 10 μm. [3] R. B. Shang, S. C. Chen, C.S. Li, and Y. Z. Zhu, "Spectral modulation interferometry for quantitative phase imaging," Biomedical Optics Express **6**(2), 473-479 (2015). Used under fair use, 2015.

Fig.3-4 shows the quantitative phase images of the resolution target obtained from the SMI system. Fig.3-4(a) shows the original interference image which need to be demodulated later.

The small image shows the zoom-in image of the selected area, which indicates that the sampling density is very high. The pathlength difference between the two arms is 1.23mm, which produces 4.72 spectral samples per cycle in the spectral direction. Fig.3-4(b) demonstrates the 2D Fourier transform of the interference image in Fig.3-4(a). It can be clearly seen that the features of the frequency components from SMI system is similar to that from conventional digital holography. The central part is the DC components which do not change with carrier frequency. With the carrier frequency, the useful signal is shifted to the position above the DC components with its conjugate part at the symmetric position. The circled part is the selected signal components for demodulation. We can see that the selected signal is already separated far enough from DC components with the current system. Fig.3-4(c) shows the 2D final OPL image of the scanning area of the resolution target. The average OPL height of the Chromium bar is 113.50 nm by our measurement. The issue of the measured height will be discussed later. Previously, we have demonstrated that the SMI system could not only measure the phase distribution of the object but also the intensity distribution of the object. Fig.3-4(d) shows the demodulated intensity image of the resolution target and Fig. 3-4(f) shows the corresponding 3D image. We can also see the background distribution of the light source from the intensity image. In order to see the detailed cross-sectional profile of the resolution target and measure the lateral resolution of the SMI system, the dashed lines (1), (2), (3) from Fig.3-4(c) and (d), respectively are shown in Fig.3-4(e). Measured from 10%~90% edge response of the OPL curve, we calculate the lateral resolution to be 0.99μm. The intensity curves and the background curves are shown in the figure below, showing that these two curves are consistent in terms of the general tendency. Therefore, in order to further deal with the intensity image, the image of the background distribution could be used to remove the background from the intensity image.

While measuring the physical height of the Cr bar on resolution target and comparing the result with commercial measurement machines, we find an interesting issue related to the quantitative OPL measurement. The upper image of Fig.3-4(e) shows the OPL measurement results from AFM and SMI before and after Ag coating on the resolution target. Using SMI before Ag coating on the resolution target, the averaged measurement result is 113.50 nm. With AFM measurement, the result is 143.15 nm. It is also confirmed by using the Dektak stylus profiler, the result of which is not shown in the figure. However, both AFM and Dektak stylus profiler are physical-contact mechanical devices, the mechanism of which is different from

optical measurement. For further comparison, an optical Zygo surface profilometer was used. The measurement result is ~126 nm, which is also not consistent with the AFM measurement result. After analyzing the discrepancy, we find that the mismatched results come from the complex reflection coefficient on the Cr-air interface. Because of the complex reflection coefficient on the Cr-air interface, the light reflected from the interface will experience an additional phase change besides the π phase shift. However, it does not happen when light reflects from the glass-air interface. Therefore, the physical height measurement derived from the phase will be different from the actual value. In order to verify this idea, we coated the entirely surface of the resolution target with Ag and measured the height again as is seen in Fig.3-5.

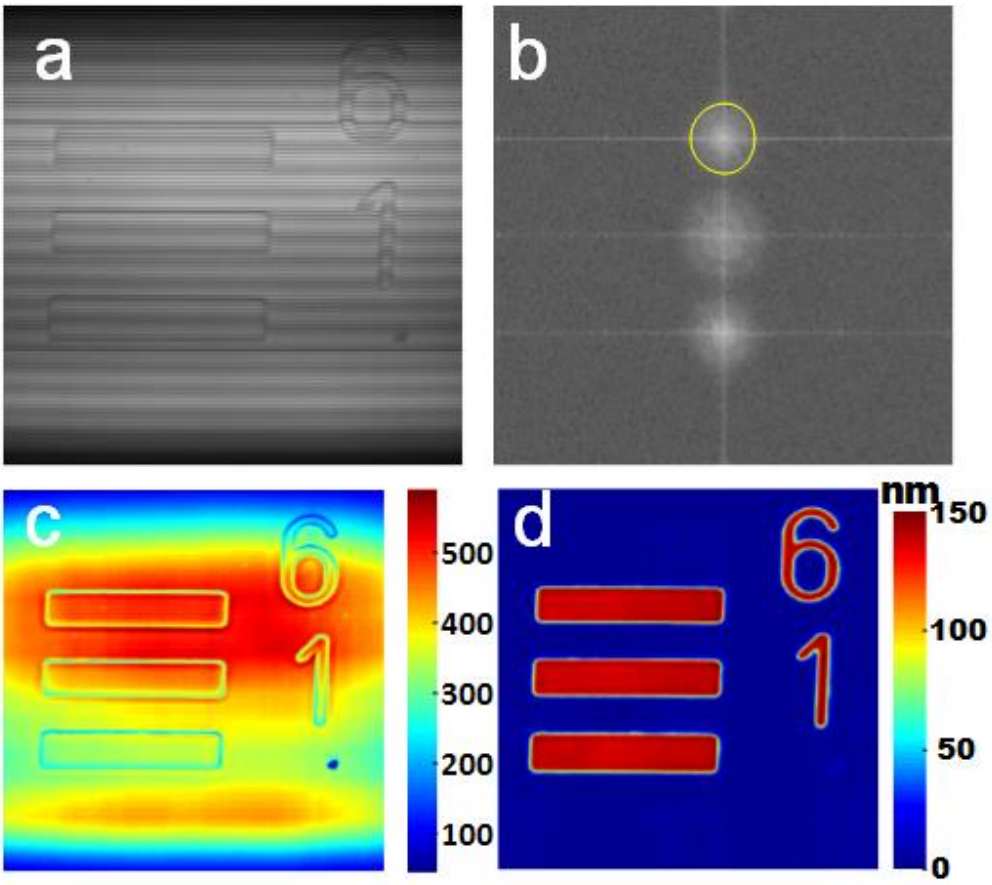

Fig.3-5 Quantitative phase imaging of the resolution target with Ag coating by SMI; (a) 2D original interferogram; (b) 2D FFT of the original interferogram in (a) with circular filter for the designated signal; (c) 2D intensity image of the coated resolution target; (d) 2D OPL image of the coated resolution target

Fig.3-5(a) and (b) show that the interferogram and the 2D FFT image almost keep the same as those from uncoated resolution target. For coated resolution target, there will be no intensity contrast because the whole surface is covered with Ag with the same reflection coefficient. It can be clearly seen from Fig.3-5(c) that the intensity on the bar area and the substrate is the same with only background intensity added on them. However, since the edge of the bar still has contrast, we can still see the edge even it is covered by Ag. This time, the averaged measured height from SMI is 138.94 nm as is seen in Fig.3-5(d), which matches well with the previous AFM measurement result. However, there is still ~5nm difference compared with the result from AFM. The main reason is the issue of system optimization. As is mentioned previously, since the Zeiss tube lens matching with the Zeiss objective is not used in the current SMI system, the system has not been in the optimal correction state. Therefore, this non-optimal correction might lead to a little measurement difference.

Previously, we have demonstrated that the SMI system has the feature of speckle-free quantitative phase measurement, which will result in a high temporal and spatial sensitivity (if the measured surface is absolutely flat). In this case, a relative flat gold mirror is used to measure both the temporal and spatial sensitivity. Since all the other parameters are fixed such as CCD camera exposure time and light source power, this experiment will show how the galvanometer scanning can affect the performance of the system. Fig.3-6 shows the results of the temporal and spatial sensitivity. In Fig.3-6(a), only central column from the image is used to measure the temporal sensitivity. Three image acquisition rates are tested in the experiment. For 0 Hz measurement, we trigger the galvanometer with 0 voltage all the time so that the line illumination will keep at the same position of the gold mirror with time going on. The range of the temporal sensitivity is from 0.1 nm to 0.17 nm with an average value of 0.12 nm using approximately 90% of the points on the line except some edge points. This is the ultimate sensitivity limit of the current SMI system. For 66.9 Hz imaging rate, each image contains 1024×1024 pixels with 0.082μm step in both spectral and scanning direction. From the Fig. 3-6(a), we can see that the curve matches well with the non-scanning curve, which means that the scanning at 66.9 Hz will not affect the temporal sensitivity of the SMI system. For 120.6 Hz imaging rate, each image contains 1024×512 pixels, meaning doubling the step in scanning direction. From the result, the corresponding curve will deviate from the non-scanning curve, with an average value of 0.17 nm. It is largely due to the galvanometer vibration at high turning

speed. Future improvement will include optimizing the galvanometer, its trigger pattern and further stabilizing the whole system while scanning. From Fig.3-6(a), we can also find that the temporal sensitivity curve is inverse proportional to the shape of the background spectrum. It matches well with the common sense that the pixel with higher intensity corresponds to higher temporal sensitivity. In this case, in order to future increase the temporal sensitivity, to increase the intensity of the light beam is another good option. Fig.3-6(b) shows the temporal sensitivities from different columns along the scanning direction with 120.6 Hz imaging rate. The result shows that the temporal sensitivity almost keeps the same at difference columns with the galvanometer scanning.

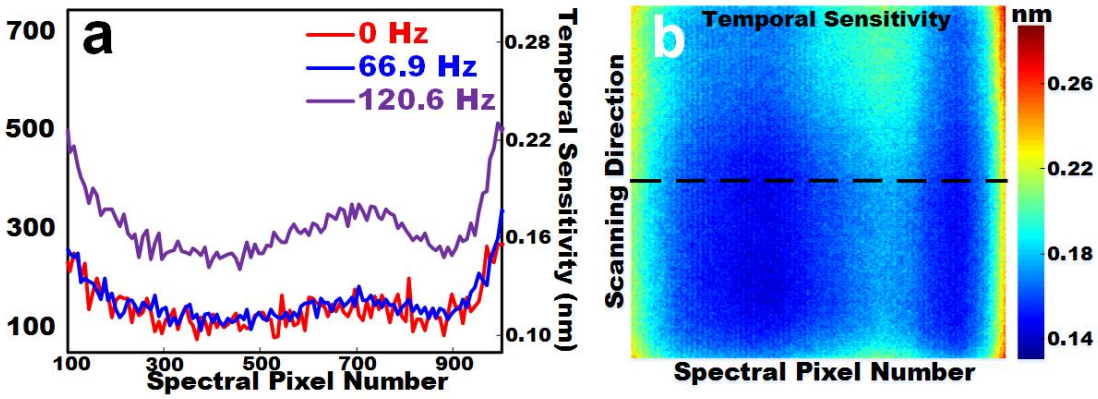

Fig.3-6 Measurement of the temporal and spatial sensitivity using gold mirror; (a) 1D temporal sensitivity measurement using the central column of the scanning image for 0 Hz, 66.9 Hz and 120.6 Hz imaging rate; (b) 2D temporal sensitivity measurement using the whole scanning image for 120.6 Hz imaging rate. [3] R. B. Shang, S. C. Chen, C.S. Li, and Y. Z. Zhu, "Spectral modulation interferometry for quantitative phase imaging," Biomedical Optics Express **6**(2), 473-479 (2015). Used under fair use, 2015.

Besides, in order to better understand sensitivity properties of the SMI system, the spatial sensitivity is also measured using the same gold mirror. Fig.3-7 shows the results. For the whole imaging area, the spatial sensitivity is 0.99 nm. For the local area within the red square, the spatial sensitivity is 0.66 nm. The reason why the spatial sensitivity is lower than the temporal sensitivity is that the surface of the gold mirror is not absolute flat. Although our system can reach ~0.1nm sensitivity for ideal case, due to the roughness of the surface of the gold mirror, the actual experimental result cannot reach the ideal value. Thus, in order to get the spatial sensitivity limit of the SMI system, a silicon wafer satisfying industrial flatness requirement could be used.

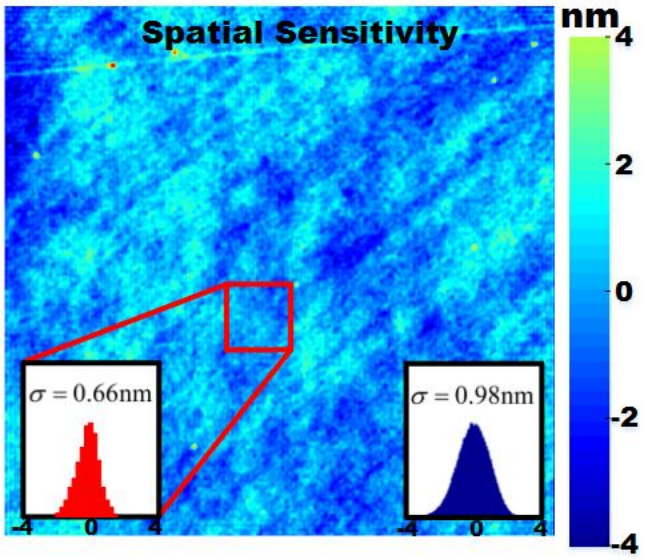

Fig. 3-7 Spatial sensitivity measurement using the whole scanning area and partial scanning area. [3] R. B. Shang, S. C. Chen, C.S. Li, and Y. Z. Zhu, "Spectral modulation interferometry for quantitative phase imaging," Biomedical Optics Express **6**(2), 473-479 (2015). Used under fair use, 2015.

From the quantitative phase measurement of the resolution target and the gold mirror, we can conclude that SMI exhibits the advantages of high resolution, speckle-free, high temporal and spatial sensitivity, and accurate quantitative phase measurement. Optimizing a few points will lead to further improvement of the SMI performance. One is that the Zeiss tube lens can be added to the system for better optical correction and more accurate quantitative phase measurement together with the Zeiss objectives. Another one is to optimize the control of the galvanometer as well as stabilizing the whole system in order to further increase the imaging rate while keeping the same sensitivity performance. Besides, originally, we have thought to get both the quantitative phase and intensity image of the uncoated resolution target. However, due to the complex reflection coefficient of the Cr-air interface, additional phase change will lead to phase measurement errors. Currently, the way to solve it is to coat the resolution target in order to obtain the same reflection coefficient throughout the surface of the resolution target. However, it will lead to the loss of intensity contrast at the same time. For uncoated resolution target, we still have the opportunity to get both the accurate phase and intensity image if we theoretically know the complex reflection coefficient of the Cr-air interface. Using the coefficient, we can calculate the additional phase shift. Then, we can subtract it from the experimental phase image to get the real phase image. Inversely, when we measure the surface profile of an unknown multi-media objects similar to the resolution target, if we know the actual physical height distribution of the

objects, using the experimental phase image from SMI, we can even calculate the reflection coefficient distribution on the surface from the actual and experimental height difference, therefore obtaining the material distribution of the measured surface. However, this idea needs further investigations.

3.3 Quantitative phase image of biological samples from SMI system

Previously, we demonstrated that SMI has the advantage of fast image acquisition rate while maintaining high temporal and spatial sensitivity. It indicates that SMI can be used to monitor and image the dynamic process of the live biological samples. Static biological samples can also be tested under SMI system. In this case, biological samples Peranema (Carolina Biological Supply), human-being cheek cell were used to test the performance of SMI system when measuring biological samples especially dynamic samples.

Firstly, we demonstrate the imaging results of the dynamic process of Peranema with SMI system. The reason we choose it as the sample is that its size is proper for the field of view of the SMI system. Besides, its motion is fast. Especially, its flagellum vibrates quickly when moving, providing a good opportunity to test SMI's dynamic imaging performance.

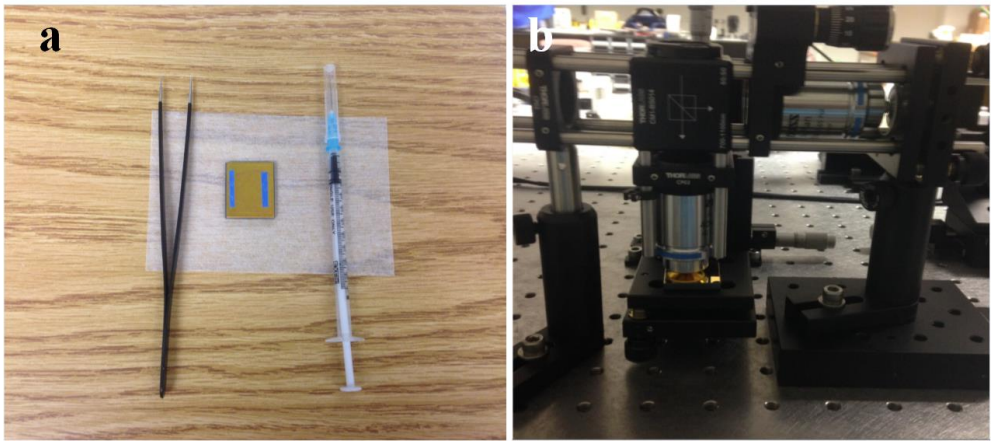

Fig. 3-8 Preparation of the biological samples for SMI system imaging

For biological samples, the procedures to prepare the sample are different from that of the resolution target. Instead of directly putting the resolution target under the objective, we need to put the samples on the surface of the gold mirror since, as mentioned previously, most of the

biological samples are transparent so that they do not provide reflection when light passes through them. Therefore, a gold mirror was used to reflect the light back. Fig.3-8 shows the preparation of the biological samples for SMI system imaging.

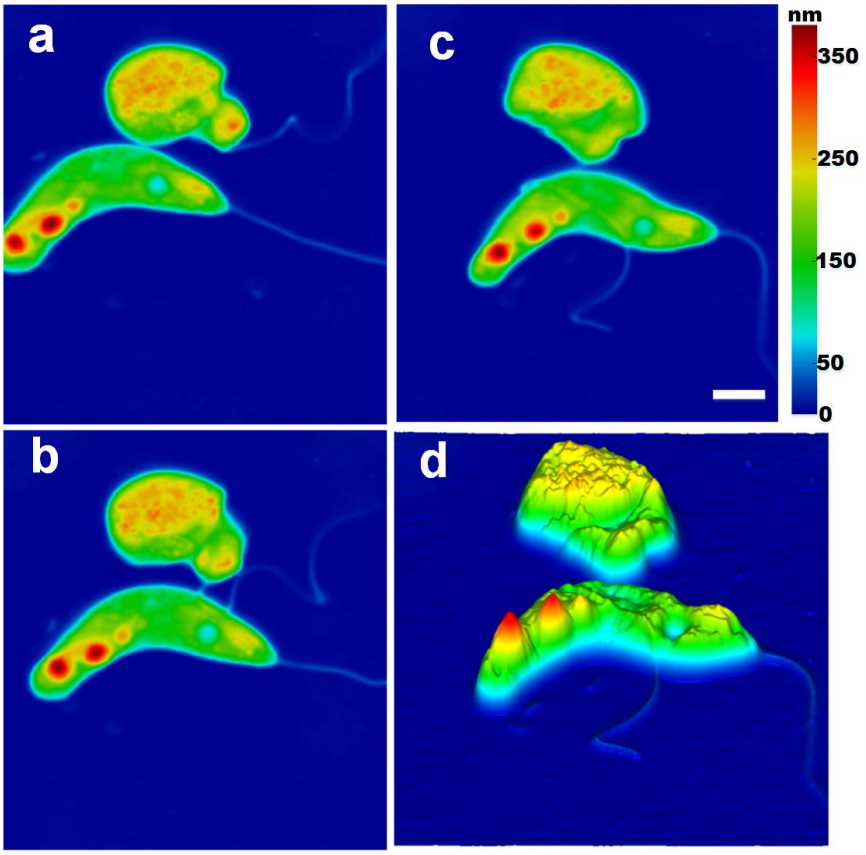

Fig.3-9 Frames of Peranema with 30 Hz imaging rate; (a) (b) (c) three frames of 2D OPL image in the dynamic process; (d) 3D OPL image corresponding to (c). Bar represents 10 μm. [3] R. B. Shang, S. C. Chen, C.S. Li, and Y. Z. Zhu, "Spectral modulation interferometry for quantitative phase imaging," Biomedical Optics Express **6**(2), 473-479 (2015). Used under fair use, 2015.

Using this method, the results will be double-pass OPL so that we need to choose half of the measured OPL as the actual OPL. After putting the biological samples on the gold mirror, a coverslip was also used to put on the top of gold mirror with the biological samples in the middle. It is like a sandwich shape. According to the experimental experience, the amount of the samples dropping on the gold mirror should be neither too much nor too little. If too much sample is dropped on the gold mirror, most of the sample will not be at the layers near to the surface of the gold mirror, which may result in light focusing issues. If too little sample is dropped on the gold mirror, when covered with a coverslip, the samples might be squeezed. Therefore, if the amount

of the sample is less than needed, use syringe to add some more samples through the edge of the coverslip. If it is too much, use the lens tissue to absorb some samples through the edge.

In the experiments, two different imaging rates are used to acquire the dynamic images. For the first experiment, the imaging rate is set as 30 Hz in the Labview program by setting some parameters. The reason why 30 Hz is chosen as the imaging rate is that it is the standard video display rate, which will be convenient for us to make the dynamic videos with the acquired serious of images. For the second experiment, we choose 120.6 Hz imaging rate which is the upper image acquisition rate limit of the current SMI system. We would like to know the performance of the SMI system to capture the dynamic processes in its upper limit status. Then, in terms of the video making, while we keep the 120.6 Hz frame rate video display, we also use 30 Hz to make a slow version of the dynamic process. Fig.3-9 shows the selected 4 frames of the dynamic process with 30 Hz imaging rate. The interaction of two Peranemas as well as the frequent vibration of the flagellum are clearly captured.

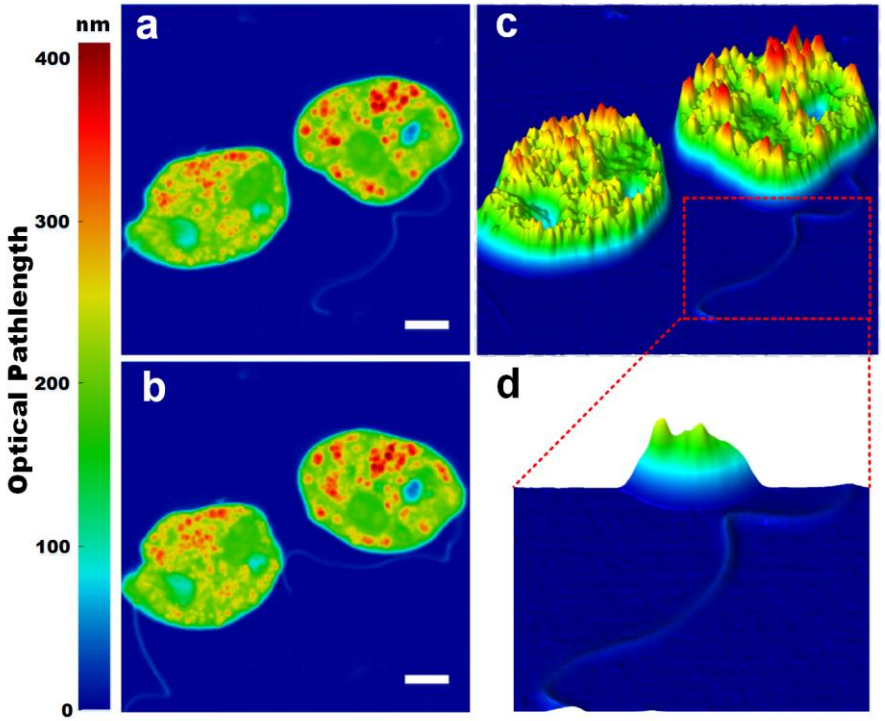

Fig.3-10 Frames of Peranema with 120.6 Hz imaging rate; (a) (b) frames of 2D OPL image in the dynamic process; (c) 3D OPL image corresponding to (a); (d) zoom-in image of the red-squared part in (c). Bar represents 10μm. [3] R. B. Shang, S. C. Chen, C.S. Li, and Y. Z. Zhu, "Spectral modulation interferometry for quantitative phase imaging," Biomedical Optics Express **6**(2), 473-479 (2015). Used under fair use, 2015.

Fig.3-10 shows the frames of another set of dynamic process with 120.6 Hz imaging rate. Both the 2D and 3D frames are shown in the figure. Besides, the zoom-in image of the red-squared part in Fig.3-10 is shown to demonstrate the high resolution and high sensitivity of the SMI system.

The principle of SMI confirms that it does not have observable speckles. However, from these frames, we can still see some background textures. These background textures come from the surface roughness of both the sample and the reference mirrors. In order to further eliminate these background textures, better gold mirrors with flatter surface could be used. For the reference arm, the mirror could be replaced by a silicon wafer while maintaining the same reflected light intensity by increasing the input power.

In order to make the video for the dynamic process, a little modification needs to be made in the Matlab program. Firstly, a while loop needs to be added to demodulate the unwrapped phase one frame by one frame. Secondly, we found that if we apply Zernike polynomial background subtraction to each frame separately, there will be a tiny background jump when making a video. The reason is that if we do the background subtraction based on each frame separately, the threshold selected for each frame might be different, which will lead to the background jump in the final video. One way to solve it is by setting the threshold the same for each frame. From our experiment, we found that during the same dynamic process captured by SMI system, the differential and the intensity threshold for each image almost keep the same with invisible variation. Thus, if we use the average differential and intensity threshold for each frame, the Zernike polynomial background subtraction for each frame will be based on the same parameter, eliminating the background jump.

Besides the dynamic measurement of the biological samples Peranema, human-being cheek cells are also used to test the SMI system's performance. To prepare the sample, the general procedures are the same as those of Peranema. The only difference is that a cotton bud was used to get the cheek cell from human being's mouth cavity. The way to put cheek cells on the gold mirror requires specific sequence. Firstly, we need to gently scrub the gold mirror with cotton bud to locate the cheek cells on the gold mirror. Secondly, a few drop of water is put on the gold mirror with syringe. The reversal order will not work since the cotton bud will absorb the water without leaving the cheek cells on the gold mirror. Fig. 3-11 (a) and (b) show the 2D and 3D OPL image of the single cheek cell. From the image, we can clearly see the tiny structures of the

cheek cell, especially its nuclei. It also indicates that the reflective index of the cheek cell's nuclei is higher than the surrounding area. If the cheek cells are put in the physiological saline to keep alive, the dynamic process of the cheek cells might also be observed in the future.

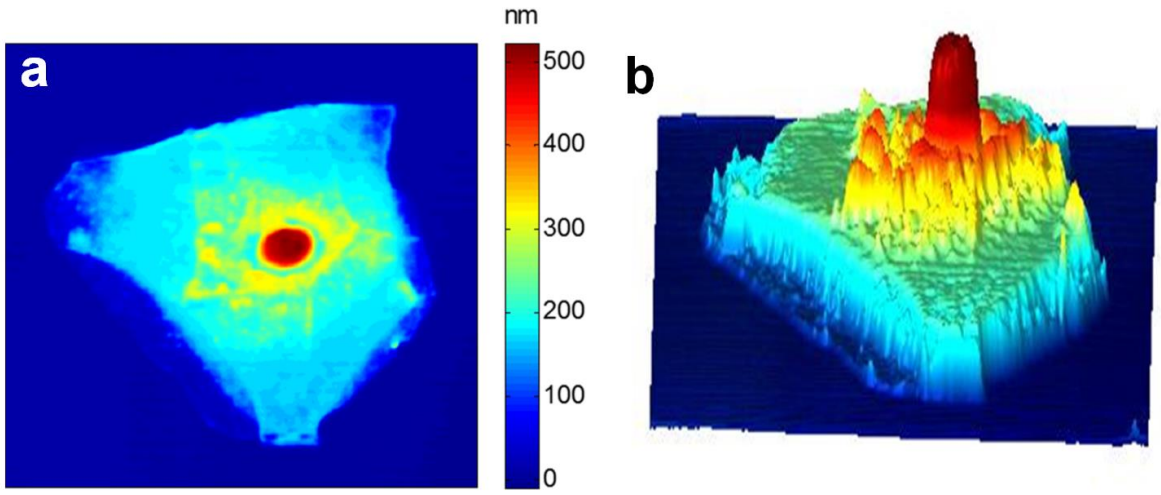

Fig. 3-11 Images of the human-being cheek cell; (a) 2D OPL image of the cheek cell; (b) 3D OPL image of the cheek cell.

3.4 References

1. G. J. Tearney, R. H. Webb, and B. E. Bouma, "Spectrally encoded confocal microscopy," Opt. Lett. **23**(15), 1152-1154 (1998).
2. L. Golan, D. Yeheskely-Hayon, L. Minai, and D. Yelin, "High-speed interferometric spectrally encoded flow cytometry." Opt. Lett. **37**(24), 5154-5156 (2012).
3. R. B. Shang, S. C. Chen, C.S. Li, and Y. Z. Zhu, "Spectral modulation interferometry for quantitative phase imaging," Biomedical Optics Express **6**(2), 473-479 (2015).
4. E. Cuche, F. Bevilacqua, and C. Depeursinge, "Digital holography for quantitative phase-contrast imaging," Opt. Lett. **24**(5), 291-293 (1999).
5. C. J. Mann, L. F. Yu, C. M. Lo, and M. K. Kim. "High-resolution quantitative phase-contrast microscopy by digital holography," Optics Express **13**(22), 8693-8698 (2005).
6. T. C. Poon, *Optical Scanning Holography with MATLAB®*. (Springer Science & Business Media, 2007).

7. T. Kreis, "Digital holographic interference-phase measurement using the Fourier-transform method," JOSA A **3**(6), 847-855 (1986).
8. D. R. Gilland, B. M. Tsui, W. H. McCartney, J. R. Perry, and J. Berg, "Determination of the optimum filter function for SPECT imaging," Journal of nuclear medicine: official publication, Society of Nuclear Medicine,29(5), 643-650 (1988).
9. R. M. Goldstein, H. A. Zebker, and C. L. Werner, "Satellite radar interferometry: Two‐dimensional phase unwrapping," Radio Science **23**(4), 713-720 (1998).

Chapter 4

Summary

In this thesis, a SMI optical system for quantitative phase imaging is demonstrated. In Chapter 1, basic concepts of quantitative phase imaging and typical quantitative phase imaging techniques are described. Firstly, the phase term is derived from Maxwell's equation and its definition is demonstrated. Secondly, the importance of phase measurement in biomedical research is demonstrated. Since most of the biological samples are transparent, they are invisible by the conventional intensity-contrast microscopy. Therefore, the phase term is regarded as a contrast to measure and image the biological samples. After this, two popular phase imaging techniques are introduced, namely Zernike phase contrast microscopy and Nomarski differential interference contrast microscopy. They are using two different mechanisms but both using the phase term as the contrast for imaging. Thirdly, the QPI is introduced. Three principles to judge the performance of a QPI technique are demonstrated, that is, image acquisition rate, resolution (transverse direction) and sensitivity (both temporal and spatial). After these, three representative QPI techniques (digital holography microscopy, phase-shifting QPI and wDPM) are introduced in detail. As a popular QPI technique, digital holography microscopy has the advantage of fast image acquisition rate, limited only by the CCD camera. However, since the coherent laser source is used, the speckle problem will show up in the demodulated phase image. Therefore, the sensitivity of digital holography microscopy will not be extremely high. Finally, the spectral imaging techniques are briefly introduced. With the use of optical diffraction devices like prisms and gratings, the spectral imaging can also be used for biomedical measurement. Usually, the information will be modulated in each wavelength of the light. Therefore, the demodulation process is to extract the information from each wavelength. SMI system exactly use the technique of spectral imaging for information modulation.

In order to better understand SMI system, in chapter 2, theoretical analysis based on diffraction theorem is made. Firstly, the theorem to analyze the coherent and incoherent optical systems is demonstrated using Fresnel diffraction. Formulas are derived for one lens system as well as 4F optical systems which is the basis of SMI system. Some simulations are also made in terms of 4F system, which is a part of the optical image processing. Then, basic formulas to

analyze SMI system are demonstrated. In fact, SMI system is a confocal optical system. Although the light source is incoherent, the whole system is still a coherent system. The complicated theorem related to optical fiber effective PSF is need for deep analysis. Here, we do not discuss it in detail. Besides, Goldstein's 2D phase unwrapping and Zernike polynomial background subtraction are introduced for image demodulation part. For most of the case, the demodulated phase image is actually a wrapped-phase image. We can tell where the phase jump is in ideal cases when no noise is introduced. However, when the noise is mixed with the real signal, the phase jump is not that easy to detect. Therefore, phase unwrapping methods are needed for exact phase extraction. Here, we use the Goldstein's 2D phase unwrapping method. It gives a reasonable way to detect the residues and how to determine the branch cuts. The details are demonstrated in Chapter 2. Due to the system aberration and non-optimal correction, even after phase unwrapping, there will still be a background on the phase image. Therefore, Zernike polynomial is used for background subtraction. Zernike polynomials use combination of some orthogonal bases to calculate the background. In SMI system, the first 8 bases are enough to extract the background within the given error. For some complex-shaped samples like Peranema we measured in the experiment, two principles are used to generate the mask for background subtraction. The first principle is using the differential information of the image to distinguish between objects and background. After first-time background subtraction, the second principle based on the intensity distribution is used to generate the second mask for the second-time background subtraction. After these two background subtraction steps, the background is removed as our expectations.

In chapter 3, the SMI system is described in detail and some relevant experiments are done with both static objects and dynamic biological samples. Firstly, the configuration of SMI system is demonstrated. As is shown in Fig. 2-1, there are mainly two 4F optical systems, a transmission grating, a galvanometer and two identical objectives to consist the SMI system. The transmission grating spreads light in one dimension and the galvanometer provides scanning in another direction, forming a 1D scanning of a line illumination. The reflected light is coupled back through the optical fiber to the spectrometer. The interference signal is acquired by the CCD camera and is sent to the computer for further processing. Secondly, Labview as well as Matlab programs for controlling and demodulating are described in details. Since we need to control the CCD camera, the galvanometer simultaneously for synchronization, Labview programs are

needed for controlling the whole process. Briefly speaking, there are two parts in the Labview program. One is the slow-scan mode and another one is fast-scan mode. In slow-scan mode, the galvanometer will scan in a low rate and the CCD camera will also be in a low image acquisition rate. This mode is usually used for sample focusing and location detecting. Once a good location of the sample is determined and moved in the center of the FOV of the objectives, the fast-scan mode will start to work. In this mode, the galvanometer will scan in a fast rate (almost upper limit) and the CCD camera will run in its optimal acquisition rate. The signal acquired from the CCD camera will be sent to the computer for data processing. In fact, the fast-scan mode is the upper speed limit of the current SMI system. Some modifications are introduced for system optimization in detail in Chapter 3. Then, experiments to test the SMI system are done with resolution target, gold mirror and biological samples. The resolution target is measured to test if the SMI system is able to measure the accurate information of the sample compared with the information from the specs (usually the height information). The gold mirror is used to measure the sensitivity performance of the SMI system. Both temporal and spatial sensitivity are calculated from the measured results to demonstrate that the SMI system has a high sensitivity performance. The dynamics of the biological sample is also measured using Peranema. The capturing of the fast movement of the Peranema indicates that the image acquisition rate of the SMI system is high enough. In summary, SMI system combines the advantages of fast scanning rate, speckle-free and high temporal sensitivity for quantitative phase measurement. With system optimization, the SMI system can have more potentials in biomedical research.

Based on this Master thesis, two papers were published as the following,

1. R. B. Shang, S. C. Chen, C.S. Li, and Y. Z. Zhu, "Spectral modulation interferometry for quantitative phase imaging," Biomedical Optics Express **6**(2), 473-479 (2015).

(It has been selected as the cover of the journal in the first publication month)

2. R. B. Shang, S. C. Chen, and Y. Z. Zhu, "High-Sensitivity Quantitative Phase Microscopy Using Spectral Encoding," Frontiers in Optics, Optical Society of America, FW4G-3 (2014).